Dynamics of an Autonomous Underwater Vehicle (AUV) towing another AUV

Omotayo Oladele

Thesis submitted to the Faculty of the
Virginia Polytechnic Institute and State University
in partial fulfillment of the requirements for the degree of

Master of Science
in
Ocean Engineering

Stefano Brizzolara, Chair
Alan Brown
Craig Woolsey
Daniel J. Stilwell

April 26, 2023
Blacksburg, Virginia

Keywords: Autonomous underwater vehicles, Vehicle dynamics, Towing Systems, Underwater cables

Dynamics of an Autonomous Underwater Vehicle (AUV) towing another AUV

ABSTRACT

Omotayo Oladele

This thesis proposes a method to simulate the dynamics of an autonomous underwater vehicle towing another autonomous underwater vehicle of equivalent size using a marine cable in the vertical and horizontal plane. There is a coupling effect between the two vehicles because the towed vehicle is of equivalent size. This means that the towed vehicle cannot be modeled as just a payload but rather, must incorporate the forces and moments experienced and acting on it. In this work, only AUVs with symmetrical hulls are considered, where the towing AUV is moving at a constant velocity with a set thrust while the towed AUV has no thrust. The rope system is another important component that needs to be modeled correctly because the rope material and type significantly impact the motion of the vehicles. The rope system in this study is modeled using a numerical approach called the lumped mass spring damper method which is easy to understand and computationally inexpensive. The rope model accounts for buoyancy differences in different ropes and permits cable flexibility. This thesis enables us to study the motion of multiple combinations of different ropes and axi-symmetric types of underwater vehicles with any fixed or movable fin configuration.

Dynamics of an Autonomous Underwater Vehicle (AUV) towing another AUV

GENERAL AUDIENCE ABSTRACT

Omotayo Oladele

This thesis studies the motion of an autonomous underwater vehicle towing another autonomous underwater vehicle which is a large as it is. The towed vehicle cannot be assumed to be just a mass attached to the towing vehicle. There is an interaction between the two vehicle. The towed vehicle places a force on the towed vehicle and the towed vehicle likewise places a force on the towing vehicle. This interaction needs to be modeled correctly to fully capture the impact of both vehicles and their appendages. Additionally, the rope system poses a huge impact on the two vehicle depending on what type of rope is selected. Multiple factors affect the performance of a rope such as the shape and the elasticity. Some ropes may also be denser due to their material type and are less buoyant than others. These factors are considered in the modeling of the overall system and allows us to study different combinations of ropes and symmetric hulled autonomous underwater vehicles.

Acknowledgements

I would like to thank my parents for supporting me through all my years of education. They have given their all to make this possible and given me the best chance at life. I am eternally grateful for them. I would like to thank the rest of my family and my friends for all the emotional support in some of the most difficult points in this program. Their words of encouragement kept me strong and helped make this possible. I also wish to thank my advisor, Dr. Brizzolara for all the countless days and hours he spent with me explaining difficult concepts and working through this thesis to make sure everything worked out. I would have never completed this thesis without his help and I am forever grateful. I would like to thank Dr. Stilwell, Dr. Woolsey and Dr. Brown for agreeing to be on this committee and for all the feedback and tips they gave me over the course of this thesis. To my lab mates at Center for Marine Autonomy and Robotics at Virginia Tech. It's been great working alongside you all and being motivated by your curiosity and tenacity. Especially Taylor Njaka and Lakshmi Miller, both of whom dedicated a lot of their time to help me better understand concepts and also review this thesis. I am grateful. Thank you all.

Contents

List of Figures

List of Tables

List of Abbreviations

ANCF	**Ansolute** and **N**odal **C**oordinate **F**ormulation
ASE	**Analytic** and **S**emi **E**mpirical
A.U.V	**A**utonomous **U**nderwater **V**ehicle
B.R.F	**B**ody **R**eference **F**rame
C.B	**C**enter of **B**ouyancy
C.G	**C**enter of **G**ravity
D.C.M	**D**irection **C**osine **M**atrix
D.O.F	**D**egrees **O**f **F**reedom
I.M.O	**I**nternational **M**aritime **O**rganisation
I.R.F	**I**nertial **R**eference **F**rame
ISimI	**I**ntegrated **S**ubmergible for **I**ntelligent **M**ission **I**mplementation
KORDI	**K**orea **O**cean **R**esearch and **D**evelopment **I**nstitute
L.M.S.D	**L**umped **M**ass **S**pring **D**amper **M**ethod
MOERI	**M**aritime and **O**cean **E**ngineering **R**esearch **I**nstitute
R.O.V	**R**emotely **O**perated **V**ehicles

Chapter 1

Introduction

Autonomous Unmanned Vehicles (AUV) have a growing demand with the desire to explore more remote areas of the ocean. Remotely Operated Vehicles (ROV) have previously been the vehicles of choice but these vehicles have to be tethered to a surface ship which presents limitations [2]. AUVs on the other hand can be deployed independently from a surface ship. AUVS can be used to complete missions such as sonar bathymetry of the ocean floor, used to collect soil sample, inspect underwater structures for damage and search for the wreckage of missing boats and airplanes. The uses of AUVs keep expanding, thus creating a desire for improvement in their range and endurance [3]. Different criteria such as energy source, speed, AUV size and the method of navigation determine the endurance of an AUV [2]. These challenges encourage the demand for innovative solutions.

This thesis is focused on solving some of the aforementioned issues, by developing a maneuvering model to study the dynamics of an AUV which tows a payload of equivalent size. This payload could be another AUV of equivalent size or a GPS sensor that stays on the surface to provide better navigation [4]. The model was developed in MATLAB rather than using commercial dynamic analysis software like Orcaflex. Orcaflex in particular does not consider the full system of the towing AUV with the rope and the cargo being towed. In Orcaflex, the system would need to be modeled as individual components and all the data from these components would need to be placed in MATLAB and solved as a system [5]. Therefore, the problem is rather all modeled in MATLAB for more flexible control of all the background processes and calculations that determine the final results.

The maneuvering model was developed in multiple phases, with the initial model solving for the motion of an individual AUV. The problem was then extended to include a rope attached to the tail of the towing AUV. The rope had a significant mass which was considered as the payload. The rope was modeled using a lumped mass spring damper model where it is divided into equal segments of N links with N+1 nodes connecting the segments together. As an extension to this model, an additional AUV was included to the system as the payload being towed. In this case, the towed AUV can be of a significant or equivalent

mass to the towing vehicle. This configuration presents some difficulty as there would be need to consider the coupling of the forces from each vehicle [6].

The maneuvering model includes three different sub systems for each component namely, the towing AUV, the towed AUV and the rope. The dynamics of the system are solved in a loosely coupled manner where the dynamics of the sub components at each time step are solved within the subsystems. After-which, the information from all the sub components of the system are incorporated and processed in a main system framework. The main system updates the sub systems with the processed dynamics of the whole system in preparation for the next time step. This process is repeated until the stopping criterion is achieved.

Chapter 2

Vehicle Dynamic Model

In this chapter, the coordinate system, the forces and the kinematics of the AUVs are discussed. The system is modeled to contain a towing AUV and a towed AUV, both of which are modeled identically.

Due to this, most equations and calculations are similar and would only differ when a specific problem is being solved or tested for. For instance, in this case the specific problem is to locate the points of attachment of the rope on the vehicles. Another specific concern may be to accommodate two crafts that are not the same.

For simplicity, this chapter will discuss the vehicle modeling for a generic AUV and the equations of each vehicle shall be highlighted with emphasis.

2.0.1 Background and Inspiration

This program was designed to be translatable to other applications and crafts. Hence a prolate spheroid was used. A lot of the assumptions that are made across the thesis can only be applied to these types of AUVs and would not accurately predict the motion of others.

The development of the program began with the model AUV as the Virginia Tech 690 AUV which can be seen in Figure (2.1). The AUV is also initially modeled to be in the horizontal plane and as such, across the thesis, a lot of concepts will be introduced pertaining to the horizontal plane. In the case where they are different from the vertical plane, hydrodynamic derivatives for the vertical plane will be specifically mentioned.

2.0.2 Reference Frames

In modeling the vehicle, two reference frames were considered. The Body Reference Frame (BRF) and the Inertial Reference Frame (IRF). BRF is the reference frame associated with the vehicle and has six degrees of freedom (DOF) as can be seen in the Figure (2.1). These

are surge, sway, heave which are the velocities and are represented by u, v, w respectively, while roll rate, pitch rate and yaw rate are the angular rates and are represented by p, q, r respectively.

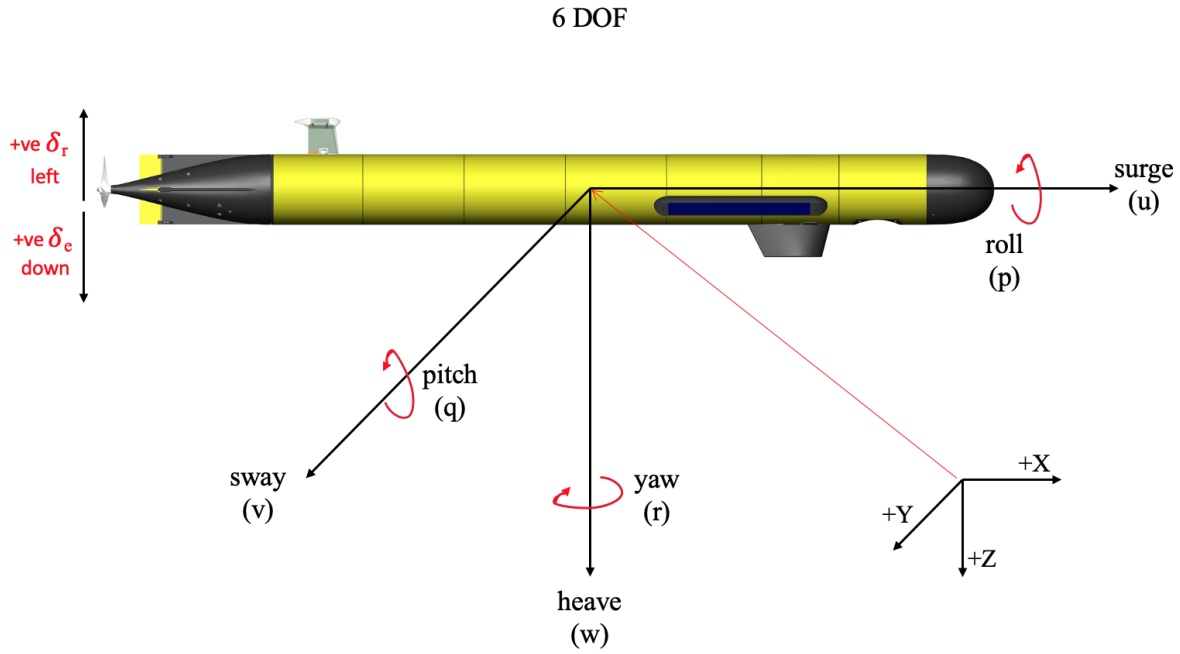

FIGURE 2.1: Body and Inertial Reference Frame representation of the Virginia Tech 690 Vehicle

In this study, only three DOF are considered at a time, as the system is constrained into the horizontal and vertical plane. The framework began with the system constrained in the horizontal plane and focused on the surge, sway and yaw velocities. The program was further extended to constrain the motion to the vertical plane to obtain the surge, heave and pitch velocities.

The BRF solves the kinematics of the vehicle wrt to the center of buoyancy of the vehicle while the IRF focuses on the position and space the vehicle is navigating in which is earth in this case. IRF has 6 DOF, x, y, z for the directions and ϕ, θ, ψ for the angles which are roll, pitch and yaw respectively [7]. When the AUV is studied in the horizontal plane, only 3 DOF are considered which are the x, y and yaw (ψ). In the vertical plane, the x, z and pitch (θ) are considered.

Adjustments are made when switching between planes, by modeling the effect of gravity in the vertical plane using COB and COG specifications. As a result, across the program x,y and ξ are symbolically used to represent the degrees of freedom in the IRF system and do not hold the true meaning of the notations mentioned above. This means the symbol y could be representing the z direction in the IRF if the study is in the vertical plane and

the symbol ξ could represent the yaw angle in the IRF when the study is in the horizontal plane.

Conversions between B.R.F and I.R.F are possible with the use of a direction cosine matrix (DCM), which is utilizes the principles of Euler rotation. This is a form of rotation where the Euler angles, roll (ϕ), pitch(θ) and yaw(ψ) are used as a way of representing a reference frame wrt to another reference frame. The Euler rotation is applied using standard vehicle navigation and control orientation in the z,y,x order [8].

The cosine and sine in the matrix have been replaced with cs and sn respectively and the full rotational matrix is shown in the matrix 2.1.

$$R_{BI} = \begin{bmatrix} cs(\theta)cs(\psi) & -cs(\phi)sn(\psi) + sn(\phi)sn(\theta)cs(\psi) & sn(\phi)sn(\psi) + cs(\phi)sn(\theta)cs(\phi) \\ cs(\theta)sn(\psi) & cs(\phi)cs(\psi) + sn(\phi)sn(\theta)sn(\psi) & -sn(\phi)cs(\psi) + cs(\phi)sn(\theta)sn(\phi) \\ -sn(\theta) & sn(\phi)cs(\theta) & cs(\phi)cs(\theta) \end{bmatrix} \tag{2.1}$$

When only 3 DOF are being considered, the rotational matrix is further simplified to only utilize the Euler angles for the degrees of freedom being considered, leading to the reduced matrices in equations (2.2) and (2.3).

$R_{BI,y}$ details the vehicle's rotation along the z axis, which transforms the vehicle's motion from the inertial reference frame to the body reference frame in the horizontal plane.

$$R_{BI,y} = R_{z,\psi} = \begin{bmatrix} \cos\psi & \sin\psi & 0 \\ -\sin\psi & \cos\psi & 0 \\ 0 & 0 & 1 \end{bmatrix} \quad R_{IB,y} = (R_{BI,y})^{-1} = \begin{bmatrix} \cos\psi & -\sin\psi & 0 \\ \sin\psi & \cos\psi & 0 \\ 0 & 0 & 1 \end{bmatrix} \tag{2.2}$$

$R_{BI,z}$ details the vehicle's rotation along the y axis, which transforms the vehicle's motion from the inertial reference frame to the body reference frame in the vertical plane.

$$R_{BI,z} = R_{y,\theta} = \begin{bmatrix} \cos\theta & 0 & -\sin\theta \\ 0 & 1 & 0 \\ \sin\theta & 0 & \cos\theta \end{bmatrix} \quad R_{IB,z} = (R_{BI,z})^{-1} = \begin{bmatrix} \cos\theta & 0 & \sin\theta \\ 0 & 1 & 0 \\ -\sin\theta & 0 & \cos\theta \end{bmatrix} \tag{2.3}$$

Orientation of Forces and Moments of the AUV

The main program contains the initial conditions of the rope and AUVs and feeds this information into the sub codes at the beginning of every time step. In the AUV sub code, most kinematic calculations are done in the body reference frame as previously mentioned. The results from these calculations are returned to the main program which solves for the position of the AUVs in the inertial reference frame and sends it into the rope sub code where the tug force on the ends of the ropes are solved. The rope sub code primarily solves in the IRF and its outputs are in the IRF. The multiple conversions between the IRF and BRF leads to the need for a conversion matrix for the tug force.

An example involves the conversion of given tug forces of the AUVs in each AUV sub system, from IRF to BRF using the DCM matrix, as depicted in equation (2.4).

$$\begin{bmatrix} F_{x_{BRF}} \\ F_{y_{BRF}} \end{bmatrix} = \begin{bmatrix} \cos\xi & \sin\xi \\ -\sin\xi & \cos\xi \end{bmatrix} \begin{bmatrix} F_{x_{IRF}} \\ F_{y_{IRF}} \end{bmatrix} \tag{2.4}$$

where $F_{x_{BRF}}$ and $F_{y_{BRF}}$ are the forces of the AUV in the x and y directions respectively, in the BRF and $F_{x_{IRF}}$ and $F_{y_{IRF}}$ are the forces of the AUV in the x and y directions respectively, in the IRF.

The simulation is modeled for the AUV tug force $F_{y_{BRF}}$ to be applied at the desired point of attachment on either AUVs. The moment arm is the distance from the point of attachment of the rope to the center of buoyancy (CB).

Knowing the moment arm is important due to the force from the rope and the moment it creates on the AUV. The location of CB in this case can be easily found using equation (2.5) because the vehicle is a symmetrical prolate spheroid.

$$CB = \frac{l_v}{2} \tag{2.5}$$

In Figure 2.2, when the rope is attached to either the nose or tail of the AUV, the moment arm, l_{arm} becomes the distance from the ends of the vehicle to the CB. Making $l_{arm} = \pm\frac{l_v}{2}$ in this case because CB is centered at midship. The lever arm sign is dependent on the direction of where the force is applied from CB. When the rope is attached at the tail of the AUV, the moment arm is negative. If the rope is attached to the CB, then l_{arm} will be 0.

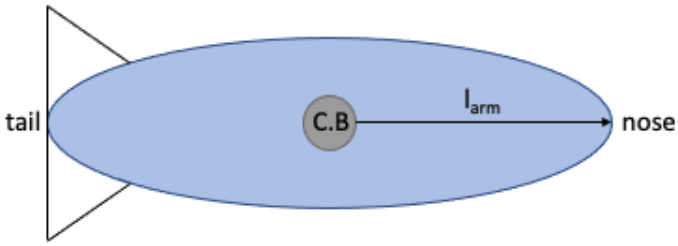

FIGURE 2.2: The moment arm runs from the center of gravity of the AUV to either ends of the AUV when the rope is attached at the ends

The induced moment created by $F_{y_{BRF}}$ acting on the vehicle is solved by using the moment equation as shown in (2.6).

$$M_{BRF} = F_{y_{BRF}} \cdot l_{arm} \tag{2.6}$$

2.0.3 Hydrodynamic Forces

The hydrodynamic forces are the forces that highlight the effect of lift and drag on the vehicle's body and its appendages. The controls on the vehicle impact these forces because changes to the orientation of the appendages can change the lift and drag profile of the vehicle. For example, changing the angle of the rudder leads to changes in the hydrodynamics of the vehicle because the lift and drag forces are proportional to the surface area of the rudder.

The lift and drag for the AUV are calculated following Kepler et al.[9] which takes inspiration from Hoerner's approximation where the vehicle is assumed to be a prolate spheroid with appendages that are flat plates [10]. The lift and drag forces of the body are determined as shown in equation (2.7)

$$F_L = -\frac{1}{2}\rho A_r C_{yd} u^2 \qquad F_D = -\frac{1}{2}\rho C_D A_{fr} |u| u \tag{2.7}$$

where ρ is the water density, C_{yd} is the lift coefficient with respect to the side slip angle β,C_D is the drag coefficient and u is the surge velocity

$$A_{fr} = \pi \cdot r_v^2 \qquad A_r = (\frac{d_v}{2})^2 \tag{2.8}$$

A_{fr} and A_r are the frontal and reference area of the vehicle respectively and r_v and d_v are the radius and diameter of the vehicle respectively.

In equation (2.9), Hoerner estimates C_{yd} by utilizing the side slip angle β and the length to diameter ratio of the vehicle as shown in equation (2.9). In equation (2.10), β can be approximated using the small angle approximation, for cases where $|u| >> |v|$.

$$C_{yd} = (\frac{180}{\pi})0.003(\frac{l_v}{d_v})\beta \tag{2.9}$$

$$\beta \approx \tan(\beta) = (\frac{v}{u}) \tag{2.10}$$

The coefficient of drag, C_D of the vehicle is a function of the Reynolds number of the body. The vehicle is assumed to be operating in a turbulent regime and C_D value is approximated using equation (2.11).

$$C_D = C_f \cdot [3(\frac{l_v}{d_v}) + 4.5(\frac{d_v}{l_v})^{1/2} + 7(\frac{l_v}{d_v})^2] \tag{2.11}$$

where $C_f = 0.004$ according to ITTC 1957 is the coefficient of friction.

Contributions from the Appendages

The hydrodynamic contributions from the fins are also determined using Hoerner's model. The lift coefficient for the fin is calculated by assuming that the lift force acts on the centroid of the fin. As given in equation (2.12).

$$C_{l_{fin}} = -\frac{1}{2}\rho A_f C_l \beta_e u^2 \tag{2.12}$$

The drag of the fin is modeled assuming a NACA 0009 airfoil profile with a C_{D_0} value of 0.0055. Hoerner solves the problem using equation (2.13).

$$C_{D_{fin}} = -4(\frac{1}{2}\rho C_{D_0} 2A_f) \tag{2.13}$$

The drag and lift contributions from the appendages are combined with the drag and lift from the body of the vehicle to determine the total drag and lift profile of the vehicle.

Sub Components of the Hydrodynamic Forces

The summation of the hydrodynamic forces from the body and appendages is partitioned into sub components. They are represented across the thesis using coefficients to show the

sub-component on which they are acting on. The coefficients are the partial derivatives of the force or moment in focus with respect to the velocity or acceleration component. The Taylor series expansion is given in equations (2.14), (2.15) and (2.16) [11][12]. Here, the terms are second order and we ignore any terms greater than second order.

$$\sum X = X_{u|u|}u|u| + X_{\dot{u}}\dot{u} + X_{wq}wq + X_{qq}qq + X_{vr}vr + X_{rr}rr + X_{prop} \tag{2.14}$$

$$\begin{aligned}\sum Y = Y_{v|v|}v|v| + Y_{r|r|}r|r| + Y_{\dot{v}}\dot{v} + Y_{\dot{r}}\dot{r} + Y_{ur}ur + Y_{wp}wp + Y_{pq}pq \\ + Y_{uv}uv + Y_{uu\delta_r}u^2\delta_r\end{aligned} \tag{2.15}$$

$$\begin{aligned}\sum N = N_{v|v|}v|v| + N_{r|r|}r|r| + N_{\dot{v}}\dot{v} + N_{\dot{r}}\dot{r} + N_{ur}ur + N_{wp}wp \\ + N_{pq}pq + N_{uv}uv + N_{uu\delta_r}u^2\delta_r\end{aligned} \tag{2.16}$$

Table 2.1 details the non zero coefficients from these equations and details what forces and moments they affect.

The forces and moments displayed are only for the XY projection. In this study, only vehicles with top-bottom (XY projection) and port - starboard (XZ projection) symmetry are considered, which allows the derivation of the XZ projection forces to be similar [12]. When converting from XY to XZ, the signs of some hydrodynamic coefficients changes due to the change in the direction in which the force is applied. The coefficients involved are shown in equations (2.17), (2.18), (2.19), (2.20) and (2.21).

$$M_{ww} = -N_{vv} \tag{2.17}$$

$$M_{uw} = -N_{uv} \tag{2.18}$$

$$Z_{qq} = -Y_{rr} \tag{2.19}$$

$$Z_{uq} = -Y_{ur} \tag{2.20}$$

$$Z_{\dot{q}} = -Y_{\dot{r}} \tag{2.21}$$

Coefficients	
Coefficient Name	Definition
N_{vv}/Y_{vv}	The partial derivative of the moment N or force Y with respect to $v \cdot \|v\|$
N_{uv}/Y_{uv}	The partial derivative of the moment N or force Y with respect to $u \cdot v$
$N_{\dot{v}}/Y_{\dot{v}}$	The partial derivative of the moment N or force Y with respect to $\dot{v}$
N_{rr}/Y_{rr}	The partial derivative of the moment N or force Y with respect to $r \cdot \|r\|$
N_{ur}/Y_{ur}	The partial derivative of the moment N or force Y with respect to $u \cdot r$
$N_{\dot{r}}/Y_{\dot{r}}$	The partial derivative of the moment N or force Y with respect to $\dot{r}$
$N_{uu\delta}/Y_{uu\delta}$	The partial derivative of the moment N or force Y with respect to $u \cdot \|u\| \cdot \delta$
$X_{uu\delta\delta}$	The partial derivative of the moment N or force Y with respect to $u \cdot \|u\| \cdot \delta \cdot \|\delta\|$
$X_{\dot{u}}$	The partial derivative of the moment N or force Y with respect to $\dot{u}$
X_{uu}	The partial derivative of the moment N or force Y with respect to $u \cdot \|u\|$

TABLE 2.1: Table displaying the meaning of the Hydrodynamic Coefficients

2.0.4 Vehicle Equations of Motion

The dynamics of the vehicle are determined by solving the equations of motion in accordance to Newton's Second Law [13]. The forces X,Y,Z of the 6 DOF equations of motion are defined in BRF terms as

$$X = m[\dot{u} - vr + wq - x_G(q^2 + r^2) + y_G(pq - \dot{r}) + z_G(pr + \dot{q})] \tag{2.22}$$

$$Y = m[\dot{v} - wp + ur + x_G(qp + \dot{r}) - y_G(r^2 + p^2) + z_G(qr - \dot{p})] \tag{2.23}$$

$$Z = m[\dot{w} - uq + vp + x_G(rp - \dot{q}) + y_G(rq + \dot{p}) - z_G(p^2 + q^2)] \tag{2.24}$$

The moments, K M and N are detailed in BRF terms for the roll,pitch and yaw respectively, as

$$\begin{aligned} K = J_x\dot{p} + (J_z - J_y)qr - (\dot{r} + pq)J_{zx} + (r^2 - q^2)J_{yz} + (pr - \dot{q})J_{xy} \\ +m[y_G(\dot{w} - uq + vp) - z_G(\dot{v} - wp + ur)] \end{aligned} \tag{2.25}$$

$$\begin{aligned} M = J_y\dot{q} + (J_y - J_z)rp - (\dot{p} + qr)J_{xy} + (p^2 - r^2)J_{zx} + (qp - \dot{r})J_{yz} \\ -m[x_G(\dot{w} - uq + vp) - z_G(\dot{u} - vr + wq)] \end{aligned} \tag{2.26}$$

$$\begin{aligned} N = J_z\dot{r} + (J_y - J_x)pq - (\dot{q} + rp)J_{yz} + (q^2 - p^2)J_{xy} + (rq - \dot{p})J_{zx} \\ +m[x_G(\dot{v} - wp + ur) - y_G(\dot{u} - vr + wq)] \end{aligned} \tag{2.27}$$

The internal forces acting on the body of the vehicle include the Inertia forces (M), Coriolis forces (C) and the Damping forces (D). Because this is a coupled system, there are external forces and moments acting on the body of each AUV. These include contributions from the rope and the other AUV. Additionally, the forces from the rudder and propeller are also included in the external forces and moments. The external forces are represented in the τ matrix. The internal and external forces on the AUV are represented in matrix form to determine the instantaneous acceleration as shown in equation (2.28).

$$M\dot{\nu} + C \cdot \nu + D \cdot \nu = \tau \tag{2.28}$$

where $\dot{\nu}$ represents the acceleration of the vehicle ($\dot{u}$,$\dot{v}$,$\dot{r}$,$\dot{w}$,$\dot{q}$) and ν represents the velocity of the vehicle (u,v,r,w,q)

When the vehicle is in the vertical plane, the effect of gravity on the vehicle is accounted for by adding a gravity force (G) to the equation.

$$M\dot{\nu} + C \cdot \nu + D \cdot \nu + G = \tau \tag{2.29}$$

Internal Forces

The internal forces are concentrated on the body of the AUV and do not incorporate interactions with other components such as the rope or other AUV.

The generalized mass Inertia Matrix consists of the rigid body inertia matrix and the added mass/inertia matrix, $M = M_{RB} + M_A$. The same format is followed for the Coriolis matrix which consists of a rigid Body and an added mass matrix in the form, $C = C_{RB} + C_A$.

The rigid body component corresponds to dry mass form of the vehicle. When the vehicle moves in water, it creates a pressure induced force due to the disturbance of the fluid [14]. This added disturbance on the surrounding fluid due to the motion of the vehicle must be accounted for and is represented as the added mass force.

Inertia Matrix

The motion of the vehicle is considered in only one plane at a time. Leading to a reduction in the degrees of freedom considered to 3 DOF. This reduces the Inertia matrix to become a 3 x 3 matrix. The Inertia matrix consists of the mass of the vehicle and the moment of Inertia. The profile of the AUV is assumed to be a cylinder when calculating the moment of inertia [9][15]. Additionally, the length of the vehicle (l_v) and radius of the vehicle (r_v) are approximated to be the length and radius of the cylinder respectively. With these assumptions, J_x, J_y, J_z can be computed using the equations (2.30).

$$J_x = \frac{1}{2} \cdot m \cdot rv^2, J_z = J_y = \frac{m}{12} \cdot [3{r_v}^2 + {l_v}^2] \tag{2.30}$$

The inertia matrix of the rigid body and added mass are detailed in equations (2.31) and (2.32) respectively. The inertia matrix of the added mass is a function of the hydrodynamic coefficients of the vehicle, which would be further detailed in later sections.

$$M_{RB,x} = \begin{bmatrix} m & 0 & 0 \\ 0 & m & 0 \\ 0 & 0 & J_z \end{bmatrix} \quad M_{RB,z} = \begin{bmatrix} m & 0 & m \cdot z_G \\ 0 & m & 0 \\ m \cdot z_G & 0 & J_y \end{bmatrix} \tag{2.31}$$

$$M_{A,x} = -\begin{bmatrix} X_{\dot{u}} & 0 & 0 \\ 0 & Y_{\dot{v}} & Y_{\dot{r}} \\ 0 & Y_{\dot{r}} & N_{\dot{r}} \end{bmatrix} \quad M_{A,z} = -\begin{bmatrix} X_{\dot{u}} & 0 & 0 \\ 0 & Z_{\dot{w}} & Z_{\dot{q}} \\ 0 & Z_{\dot{q}} & M_{\dot{q}} \end{bmatrix} \tag{2.32}$$

$$M = M_{RB} + M_A \tag{2.33}$$

Coriolis / Centrifugal Force Matrix The rigid body component of the coriolis force is represented in equation (2.34).

$$C_{RB,x} = \begin{bmatrix} 0 & 0 & -m \cdot v \\ 0 & 0 & m \cdot u \\ m \cdot v & -m \cdot u & 0 \end{bmatrix} \quad C_{RB,z} = \begin{bmatrix} 0 & 0 & m \cdot w \\ 0 & 0 & -m(z_G q + u) \\ -m \cdot w & m(z_G q + u) & 0 \end{bmatrix} \tag{2.34}$$

The system is modeled to incorporate the added mass component of the coriolis force as shown in equation (2.35).

$$C_{A,x} = -\begin{bmatrix} 0 & 0 & -(Y_{\dot{v}} \cdot v + Y_{\dot{r}} \cdot r) \\ 0 & 0 & X_{\dot{u}} \cdot u \\ (Y_{\dot{v}} \cdot v + Y_{\dot{r}} \cdot r) & -X_{\dot{u}} \cdot u & 0 \end{bmatrix} \tag{2.35}$$

$$C_{A,z} = -\begin{bmatrix} 0 & 0 & (Z_{\dot{w}} \cdot w + Z_{\dot{q}} \cdot q) \\ 0 & 0 & -X_{\dot{u}} \cdot u \\ -(Z_{\dot{w}} \cdot w + Z_{\dot{q}} \cdot q) & X_{\dot{u}} \cdot u & 0 \end{bmatrix} \tag{2.36}$$

$$C = C_{RB} + C_A \tag{2.37}$$

Damping Matrix

The damping matrix contains the effects of the hydrodynamic lift and drag affecting the vehicle. When the vehicle is moving at lower speeds, the drag forces will have a larger effect on the vehicle than the lift forces.

The damping matrix is shown in equations (2.38) and (2.39) with the corresponding hydrodynamic coefficients that correlate to the damping forces on the vehicle.

$$D_x = \begin{bmatrix} X_{uu} \cdot |u| & 0 & 0 \\ 0 & Y_{vv} \cdot |v| + Y_{uv} \cdot u & Y_{rr} \cdot |r| + Y_{ur} \cdot u \\ 0 & N_{vv} \cdot |v| + N_{uv} \cdot u & N_{rr} \cdot |r| + N_{ur} \cdot u \end{bmatrix} \tag{2.38}$$

$$D_z = \begin{bmatrix} X_{uu} \cdot |u| & 0 & 0 \\ 0 & Z_{ww} \cdot |w| + Z_{uw} \cdot u & Z_{qq} \cdot |q| + Z_{uq} \cdot u \\ 0 & M_{ww} \cdot |w| + M_{uw} \cdot u & M_{qq} \cdot |q| + M_{uq} \cdot u \end{bmatrix} \tag{2.39}$$

Gravity Matrix

Gravity is included on both AUVs and the rope when the system is rotated to the vertical plane. The effect due to gravity on the rope is discussed in Chapter 3. The AUV requires an additional component included when modeling the effect of gravity on the vehicle. The component is the hydrostatic restoring moment. The hydrostatic restoring moment is a function of z_G, which is the distance of the Center of Gravity of the vehicle (CG) from its Center of Buoyancy (CB) as shown in equation (2.40). z_G is an important parameter when quantifying the stability of a vehicle. A greater separation distance, z_G creates a larger rocking force which could cause the vehicle to become unstable and frequently pitch up or down. For an AUV towing relatively heavy cargo or another AUV, z_G should be an important criteria to determine if a vehicle can complete a given mission.

The gravity force is shown in the matrix equation (2.40)

$$G = \begin{bmatrix} 0 \\ 0 \\ -g \cdot m \cdot sin(\theta) \cdot z_G \end{bmatrix} \tag{2.40}$$

External Forces

The external forces involve the thrust force from the propellers and the input from the appendages such as the rudder. Changes in the controls of the appendages such as prescribing a certain rudder deflection angle alter the lift or drag profiles of the appendages. The drag force on the appendages can become significantly greater and highlights the importance of modeling the inputs from the appendages accurately. The external forces are detailed in the τ matrix in equation (2.41).

Additionally, the τ matrix incorporates the tug force of the AUVs on the rope which are concentrated in the nodes at the ends of the rope. The rope forces on the first and the last nodes of the rope represent the tug forces of the towing and towed auv respectively. In the case of the towing vehicle, the tug force is the combination of all the rope forces acting on the first node of the rope. The tug force relating to the towed vehicle incorporates all the rope forces acting on the last link of the rope. The tug force of the AUV in focus is determined from the the rope sub code. In chapter 4 the flow chart of the system is discussed to detail the order of processes. At the start of the program, the tug force is

zero because the system begins from rest. This initial zero value is used to solve for the AUV kinematics in the AUV sub code to obtain their accelerations and velocities. The accelerations and velocities of the AUVs will be used to solve for the rope tug force in the next time step of the rope sub code.

The process is repeated for each time step and this new tug force output from the rope sub code becomes the tug force for the next time step of the AUV sub code. It is applied in the τ matrix of the AUV sub code as shown in equation (2.41)

The τ matrix also incorporates the induced moment from equation (2.6) which is due to the tug force can be seen in the last row of the τ matrix.

$$\tau = \begin{bmatrix} F_T + F_{x_{BRF}} + [X_{uudd} \cdot u|u| \cdot (\delta_r)^2] \\ F_{y_{BRF}} + [Y_{uud} \cdot u|u| \cdot (\delta_r)] \\ M_{BRF} + [N_{uud} \cdot u|u| \cdot (\delta_r)] \end{bmatrix} \tag{2.41}$$

where F_T is the Thrust force, X_{uudd},Y_{uudd},N_{uudd} are the rudder hydrodynamic coefficients which are explained further in the table in appendix A, δ_r is the prescribed rudder deflection angle.

Chapter 3

Rope Dynamic Model

Marine cables are difficult to model and analyze because they are very nonlinear due to the effects of the fluid drag force acting on them and their geometric configuration [16]. Numerical approaches are the only readily available methods of solving this problem. The rope tugging the towed AUV is modeled using a finite element approach, lumped mass spring damper (LMSD) method. The lumped mass spring damper method is straightforward, versatile and not computationally expensive. In this method, the total mass of the rope is divided into equally spaced mass segments along the rope.

Accurately defining the boundary conditions in this method is vital to the performance of the method. Furthermore, the boundary conditions must be followed throughout the process to avoid error in the results. In this work, the segments of the rope are called the rope links. Every two adjacent links are connected by circular joints called nodes as shown in Figure 3.1. The mass of each rope segment is concentrated in the nodes immediately behind them. While the links possess the forces, positions, velocities and angles, from which the kinematics of the segments can be calculated.

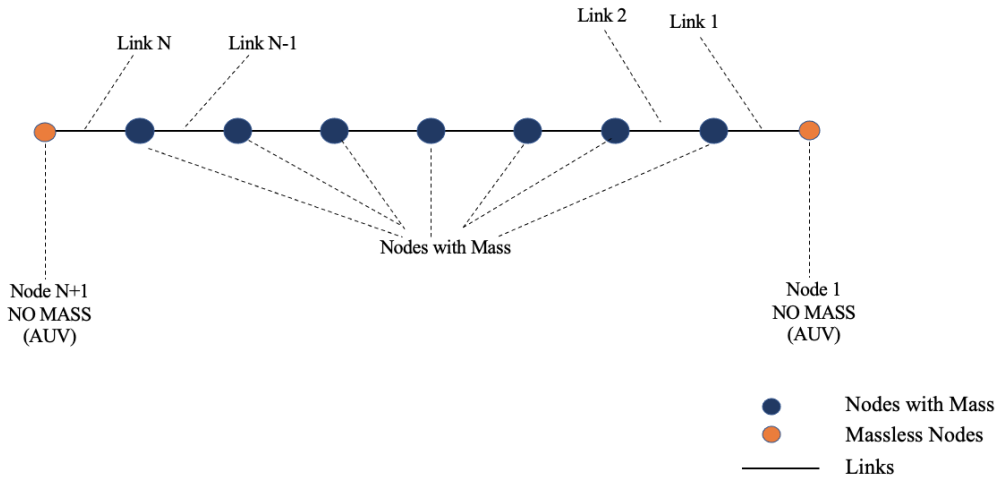

FIGURE 3.1: Rope featuring N nodes and N+1 total links with N-1 links with masses, where the orange colored links on the ends connect to the AUVs

The rope system is modeled to comprise of N+1 nodes and N links. The AUVs are included in the N+1 nodes because they are modeled as the nodes at the ends of the rope. Additionally, the nodes for the AUVs only carry forces but do not bear any masses. They can be seen in figure 3.2 where the orange nodes are shown as the AUV connection points. Because the mass of a rope segment is concentrated in the node that immediately follows it, this means that the N_{th} rope segment will not bear a mass because its node is an AUV node. The program is modeled to cut off the forces and moments for this last rope segment for all N.

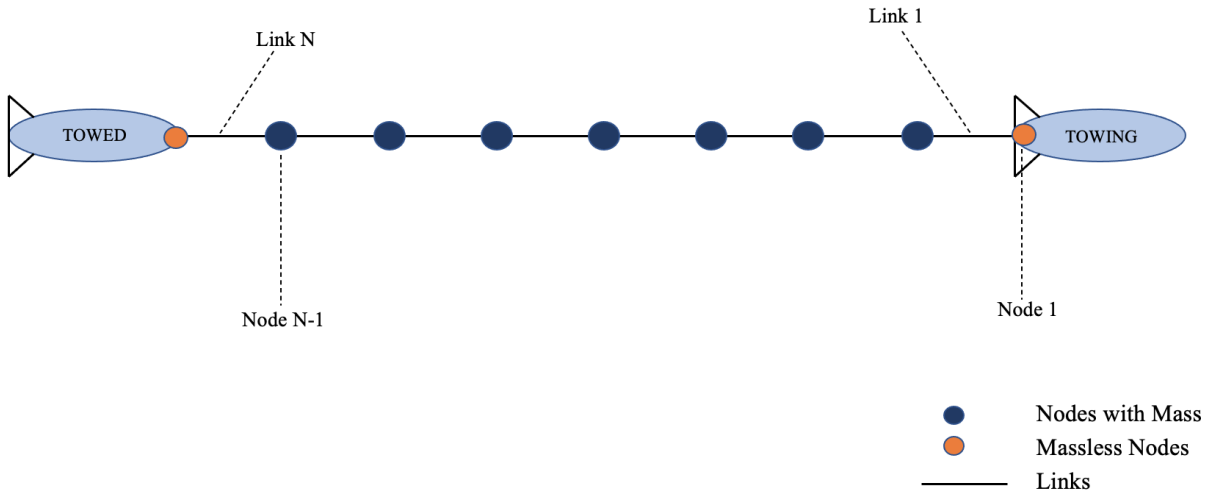

FIGURE 3.2: Configuration of rope connecting AUVs. Orange links on the ends are massless as they are in the AUVs

The mass of each rope segment is calculated to reflect the last rope segment being cut off. The mass of the whole rope is divided by N-1 rather than N, as shown in equation (3.1)

$$m_l = \frac{m_r}{N-1} \tag{3.1}$$

where m_l = Mass of Rope Segment, m_r = Rope Mass

The length of each rope segment is determined by dividing the total length of the rope by the number of segments in the rope, as detailed in (3.2).

$$l_l = \frac{l_r}{N} \tag{3.2}$$

where N = number of segments, l_l = Link Length, l_r = Rope Length

3.0.1 Coordinate System

The motion of the full AUV-Rope system incorporates multiple components which undergo multiple conversions between the different coordinate systems. Due to the loosely coupled nature of the full AUV-Rope system, the rope's motion depends on the other components and requires coordinate system conversions. The aim is for these coordinate system conversions to be as easy to comprehend and straight forward as possible. The rope's motion calculation is convoluted and confusion may arise if not careful. The rope follows two coordinate systems like the AUVs, Body Reference Frame (BRF) and the Inertial Reference Frame (IRF).

Figure 3.3 denotes the conversion of coordinates system. Across the program, the link attack angles α_l, link orientation θ_l and link heading ψ_l are used to convert the node and link coordinate systems for the forces and velocities of the link.

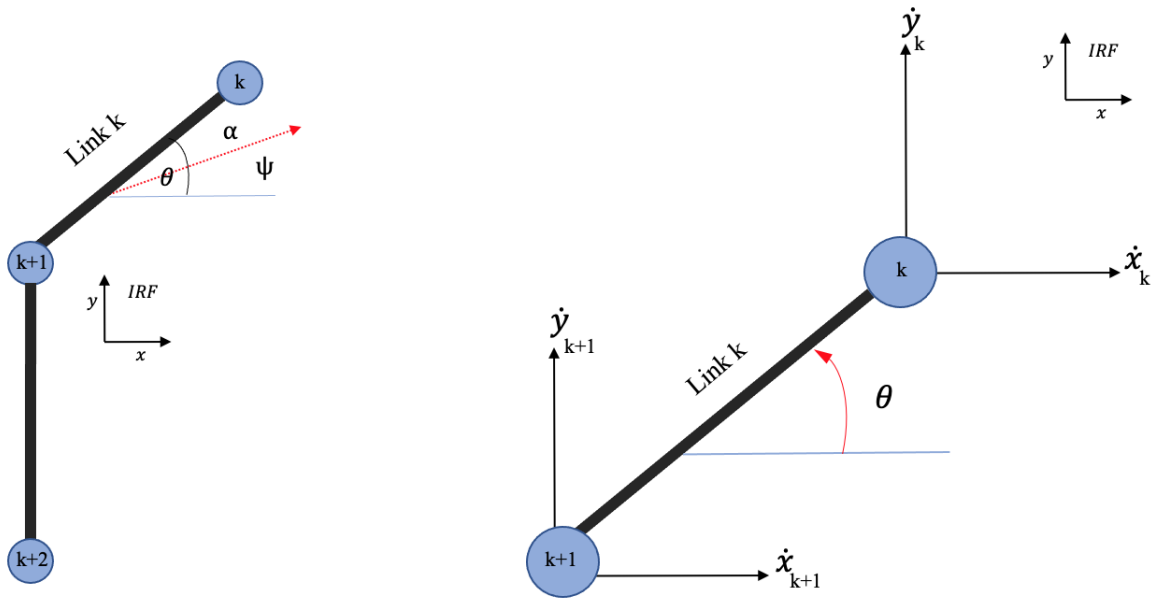

FIGURE 3.3: Schematic of coordinate system of the rope nodes.

3.0.2 Dynamic Equations

Node Position and Velocity

The rope dynamics are derived mathematically using the position of the links to obtain the angle and velocity of the rope. The position of each link j is calculated by solving the average of the position of the node k behind link j and the node k+1 which is ahead of link j. The approach is detailed in equation (3.3) and is applied to all the nodes and links to obtain the position of the whole rope.

$$x_{l^j} = \frac{x_{n^k} + x_{n^{k+1}}}{2} \qquad y_{l^j} = \frac{y_{n^k} + y_{n^{k+1}}}{2} \tag{3.3}$$

where x_{l^j} and y_{l^j} are the x and y position of the j^{th} link and x_{n^k} and y_{n^k} are the x and y position of the k^{th} node.

Similarly, the same averaging method is implemented to obtain the velocity of the links.

$$\dot{x}_{l^j} = \frac{\dot{x}_{n^k} + \dot{x}_{n^{k+1}}}{2} \qquad \dot{y}_{l^j} = \frac{\dot{y}_{n^k} + \dot{y}_{n^{k+1}}}{2} \tag{3.4}$$

where $\dot{x}_{l^j}$ and $\dot{y}_{l^j}$ are the velocity in the x and y direction of the j^{th} link and $\dot{x}_{n^k}$ and $\dot{y}_{n^k}$ are the velocity in the x direction of the k^{th} node.

The instantaneous heading, ψ_l and orientation, θ_l of the link are functions of the position of the links . The link heading is the direction in which the center of mass of each link is moving towards. While the link orientation is the angular position of the link in space. The attack angle α_l is the difference between the link heading and the link orientation. α_l represents the angle of the body relative to the fluid around it, which is water in this case.

$$\alpha_l = \theta_l - \psi_l \tag{3.5}$$

where α_l is the link attack angle, θ_l is the link orientation and ψ_l is the link heading.

θ_l and ψ_l are determined using the four quadrant inverse tangent with the atan2 function in Matlab. This approach ensures that the angles are solved for accurately based on the quadrant in which the motion occurs in. This method utilizes the x and y positions of the link and determines which equation is used, as shown in (3.6).

$$atan2(y,x) = \begin{cases} \tan^{-1}(\frac{y}{x}) & x > 0 \\ \tan^{-1}(\frac{y}{x}) + \pi & x < 0 \text{ and } y \geq 0 \\ \tan^{-1}(\frac{y}{x}) - \pi & x < 0 \text{ and } y < 0 \\ \frac{\pi}{2} & x = 0 \text{ and } y > 0 \\ \frac{-\pi}{2} & x = 0 \text{ and } y > 0 \\ \text{undefined} & x = 0 \text{ and } y = 0 \end{cases} \tag{3.6}$$

Considering the four quadrants, the orientation angle of each link is calculated by calculating the inverse tangent of the difference between the positions of adjacent nodes as shown in (3.7)

$$\theta_l{}^j = atan2(y_{n^k} - y_{n^{k+1}}, x_{n^k} - x_{n^{k+1}}) \tag{3.7}$$

Furthermore, the four quadrant inverse tangent is employed to determine the link heading. Here the method utilizes the x and y velocities of the nodes.

$$\psi_l{}^j = atan2(\frac{\dot{y}_{n^k} + \dot{y}_{n^{k+1}}}{2}, \frac{\dot{x}_{n^k} + \dot{x}_{n^{k+1}}}{2}) \tag{3.8}$$

With knowledge of the link orientation θ_l, the angular velocity of the links may be determined, since it is a function of θ_l. The angular velocity is a vital component for calculating the angular drag experienced by the rope. In equation (3.9), the formulation to determine the angular velocity of each link is detailed.

$$\dot{\theta}^j = \frac{[(\dot{y}_{n^k} - \dot{y}_{n^{k+1}}) \cdot \sin\theta_l{}^j + (\dot{x}_{n^k} - \dot{x}_{n^{k+1}}) \cdot \cos\theta_l{}^j]}{l_l} \tag{3.9}$$

where $\dot{\theta}^j$ is the angular velocity of the link

3.0.3 Rope Forces

There are internal and external forces acting on the rope. The rope is modeled as a spring mass damper and the internal forces include the tension and damping forces acting on the rope. While the external forces comprise of a drag force due to the rope's immersion in a fluid and the induced moment due to induced drag.

In the horizontal plane, the rope assumed to be neutrally buoyant which means the gravity and buoyancy forces are equal and opposite. Allowing us to exclude the gravity and buoyancy forces from the force equations in the horizontal plane. In the vertical plane, gravity and buoyancy forces are included to completely model the rope forces. The ratio of the gravity force to the buoyancy force can be specified based on the rope material employed. This option is included because rope materials vary, as do their densities. To allow a more robust rope system, the density of a given rope is taken into account and compared to the density of water to find this gravity to buoyancy ratio, which we identify as the percentage of buoyancy.

$$P_b = \frac{(\rho_{water} - \rho_{rope})}{\rho_{rope}} \cdot 100 \tag{3.10}$$

where P_b is the percent buoyancy and ρ_{water} and ρ_{rope} are the densities of water and rope respectively

Internal Forces

Tension

The tension force in the program includes the elastic tension and the viscous tension forces. The viscous tension force is due to the damping effect on the rope while the elastic tension is due to the spring-like nature of the rope. The axial tension comprises of these two forces as shown in equation (3.11). The tension force is modeled following Huang's findings in [16].

$$T_a = T_e + T_v \tag{3.11}$$

where T_a = Axial Tension, T_e = Elastic Tension, T_v = Viscous Tension

The elastic tension force is derived using Hooke's law that states that the tension force is proportional to the size of the deformed area. The deformed area can be determined by assuming the rope is a cylinder and the deformed area is the cross sectional area of the cylinder as shown in equation (3.12).

$$A_r = \pi r_r^2 \tag{3.12}$$

Following the findings of Huang, the elastic tension (T_E) is given by equation (3.13).

$$T_e = EA_r \cdot l_{sr} \tag{3.13}$$

where E is the Young's modulus of the rope material and l_{sr} is the stretch ratio of the links.

Employing the stretch length of the links, the stretch ratio of the links can be determined. In equation(3.14) the stretch length of each rope segments is calculated from the position of the two nodes attached to each link.

$$l_{ls} = \sqrt{(x_{n^k} - x_{n^{k+1}})^2 + (y_{n^k} - y_{n^{k+1}})^2} \tag{3.14}$$

where l_{ls} is the stretched length of the rope segment

With knowledge of the stretched link length at each instant, the stretch ratio can be calculated by finding the difference of the unstretched link length and the stretched link

length.

$$l_{sr} = \frac{l_{ls} - l_l}{l_l} \tag{3.15}$$

The viscous tension force which behaves as a dampening force is calculated by multiplying the link stretch velocity by the internal viscous damping coefficient, C_v . C_v is dependent on the type of rope utilized and must be specified accordingly to accurately determine the viscous tension. Selecting a rope with a large or inadequate C_v value for the chosen AUVs in a given mission will lead to issues in the simulation.

$$T_v = C_v \cdot l_{SV} \tag{3.16}$$

The direction in which T_v acts is dependent on the direction in which the links are being stretched and must be preserved. To derive the appropriate sign of the stretch velocity of the rope segments, the approximate result of the position of the links at the next time step is solved for using a very small time step, Δt_D of 1e-20 with Euler's Method for each link.

$$x_{t+1} = x_t + \dot{x}_t \cdot \Delta t_D \qquad y_{t+1} = y_t + \dot{y}_t \cdot \Delta t_D \tag{3.17}$$

where $\dot{x}_{t+1}$ and $\dot{x}_{t+1}$ represents the position of each node at time t in the x and y component.

Furthermore, the magnitude of the stretched length of the link for the next time step l_{ls}^{t+1} is calculated using the norm function in Matlab

$$l_{ls}^{t+1} = ||x_{t+1}, y_{t+1}|| \text{... for each link k} \tag{3.18}$$

Finally, the link stretch velocity can be solved for by using the sign of the difference of the stretched length at time t and that of the next time step, time $t + 1$

$$l_{SV} = sign(l_{ls}^{t+1} - l_{ls}^{t}) \cdot \sqrt{(\dot{x}_{n^k} - \dot{x}_{n^{k+1}})^2 + (\dot{y}_{n^k} - \dot{y}_{n^{k+1}})^2} \tag{3.19}$$

where l_{SV} is the Link Stretch Velocity

The total axial tension force is computed as detailed in equations (3.11). The total axial tension force finally needs to be converted from the links to the nodes and from the BRF to the IRF.

$$T_{a_x}^k = T_a^j \cdot \cos\theta_l^j - T_a^{j+1} \cdot \cos\theta_l^{j+1} \tag{3.20}$$

$$T_{a_y}^k = T_a^j \cdot \sin\theta_l^j - T_a^{j+1} \cdot \sin\theta_l^{j+1} \tag{3.21}$$

where $T_{a_x}^k$ and $T_{a_y}^k$ are the total axial tension force of the k^{th} node and $T_{a_x}^j$ and $T_{a_y}^j$ are the total axial tension force of the j^{th} link.

External Forces

Fluid Drag

The drag on the rope is resolved into two components, the tangential drag and normal drag. Both components are functions of the velocities of the links and their respective drag coefficients [16].

The tangential drag coefficient is modeled following Kepler in [9], which draws inspiration from findings in Reid and Wilson [17].

$$C_t = 2 \cdot (\frac{C_{vk}}{\ln(\frac{120}{s/R_r})})^2 \tag{3.22}$$

where $C_{vk} = 0.4$ is the von Karman constant, and s is the surface roughness diameter.

The modeling of the normal drag coefficient uses Kamman's findings for the normal drag coefficient C_n^j [18]. C_n^j is dependent on the flow regime in which the rope travels in. The flow regime may be determined using the Reynolds Number (Re) of each link as shown in (3.23) The Reynolds number is a function of the velocity of the AUVs and the rope.

$$Re_j = \frac{\rho D_r |\dot{y}_{l^j}|}{\mu} \tag{3.23}$$

where ρ is the density of water, D_r is the diameter of the rope and μ is the dynamic viscosity of the water.

Kamman details a criteria for C_n^j based on the flow regime from which the correct C_n^j value can be matched with its respective Reynolds number.

$$C_n^j = \begin{cases} 0 & Re_j \leq 0.1 \\ 0.45 + \frac{5.93}{(Re_j)^{0.33}} & 0.1 < Re_j \leq 400 \\ 1.27 & 400 < Re_j \leq 10^5 \\ 0.3 & Re_j > 10^5 \end{cases} \tag{3.24}$$

Furthermore, once the tangential and the normal drag for the rope are identified, the drag is initially solved in the BRF using the equations from [18] in (3.25)

$$\begin{bmatrix} D_{bfx} \\ D_{bfy} \end{bmatrix} = \begin{bmatrix} -\frac{\rho\pi D_r l_l C_t |\dot{x}_{nj}| \dot{x}_{nj}}{2} \\ -\frac{\rho\pi D_r l_l C_n^j |\dot{y}_{nj}| \dot{y}_{nj}}{2} \end{bmatrix} \tag{3.25}$$

The link orientation is then employed to enable the conversion of the drag force from BRF to IRF. The conversion is performed to ease the summation of all the forces.

$$D_x^j = D_{bfx} \cdot \cos(\theta_l) - D_{bfy} \cdot \sin(\theta_l) \qquad D_y^j = D_{bfy} \cdot \cos(\theta_l) + D_{bfx} \cdot \sin(\theta_l) \tag{3.26}$$

where D_x^j is the drag in the x direction of the j^{th} link and D_y^j is the drag in the y direction of the j^{th} link.

Fluid Drag Moment

The fluid drag force on the rope creates an induced moment. This moment can be determined by assuming the rope segments are beams with a load acting on them. The load in this case, is the fluid drag force on the rope.

Figures 3.4 and 3.6 illustrate the two possible settings that occur as the rope travels. The first setting includes motion in which the rope may initially only experience a linear drag force from constant flow. In this setting, there is no moment force acting on the rope and the rope is not rotating, as shown in Figure 3.4.

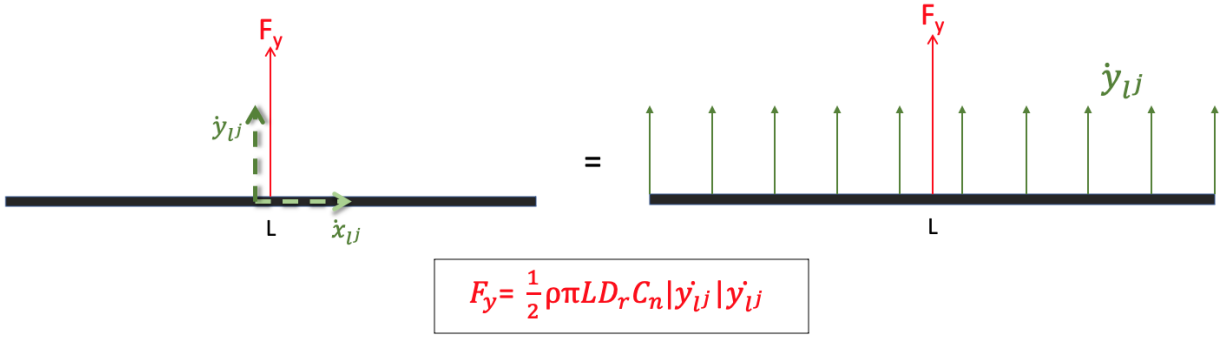

FIGURE 3.4: Illustration of a rope segment when the rope is not rotating and the fluid flow is uniform.

The second setting involves motion where the rope segment is rotating due to the drag force acting on it. In this setting, the velocity across the rope segment is non uniform and

causes the drag force acting across the rope segment to be variable. The moment in this setting is a function of the drag force. In Figure 3.6, the moment is derived. The lever arm in which the force acts on is represented by s, which runs from the center to the right end of the segment.

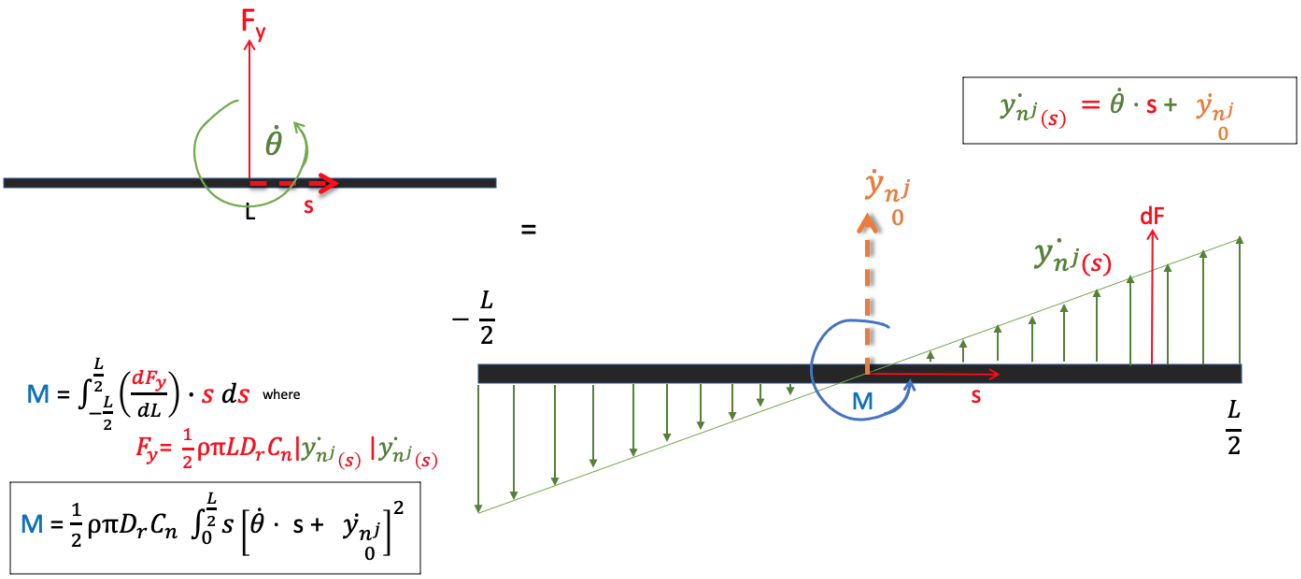

FIGURE 3.5: Illustration of a rope segment when the rope has a moment and is rotating and the fluid flow is variable.

The angular drag force found from this derivation is given by

$$l_{AD}^{j} = \rho D_r C_n \cdot [-\frac{l_l^4}{64}(\dot{\theta}^j \dot{\theta}^j) + \frac{l_l^3}{12}(\dot{y}_{lj} \cdot \dot{\theta}^j) + \frac{l_l^2}{8} \cdot \dot{y}_{lj}] \tag{3.27}$$

where l_{AD}^{j} is the angular drag

The angular drag for the links is further employed to calculate the induced moment force acting on the links. The sensitivity of the type of rope used is highlighted here because more rigid materials like steel will possess a bending resistance. The bending moment (Mo_b) is added to the angular drag to capture the total angular moment force on each link.

$$l_{AM} = l_{AD}^{j} + Mo_b \tag{3.28}$$

where l_{AM} is the Node angular Moment and Mo_b is the bending moment of the material

The total moment force on each link with mass is calculated by using the angular moment of the nodes and the orientation of the links, which decomposes the angular moment into

its x and y components in the IRF. Total moment force on the links is converted to the total moment force on the nodes to be used when solving for the acceleration of the rope. This is done because the mass is concentrated in the node and we employ Newton's second law to determine the acceleration. The conversion is performed by finding the total moment force difference between neighbouring nodes.

$$M_x^k = \frac{l_l[l_{AM^j} \cdot \sin {\theta_l}^j - l_{AM^{j+1}} \cdot \sin {\theta_l}^{j+1}]}{2} \tag{3.29}$$

$$M_y^k = \frac{l_l[-l_{AM^j} \cdot \cos {\theta_l}^j + l_{AM^{j+1}} \cdot \cos {\theta_l}^{j+1}]}{2} \tag{3.30}$$

where M_x^k is the moment in the x direction acting on the k^{th} node and M_y^k is the moment in the y direction acting on the k^{th} node.

Gravity and Buoyancy Forces In the vertical plane, each rope segment experiences gravity and buoyancy forces which are acting on it. When the rope is neutrally buoyant, both forces are equal and opposite. Otherwise, the balance of these forces is concentrated in the percent buoyancy of the rope material. The percent buoyancy can be calculated using equation (3.10).

Using a rope whose material is denser than water such as steel will have a greater gravity force effect than that of a synthetic fiber rope which is less dense. The synthetic fiber rope contrarily, will possess a greater buoyancy force effect. The equation for the gravity and buoyancy force balance is given in equation (3.31)

$$gb = \pm \frac{P_b}{100} \cdot m_l \cdot g \tag{3.31}$$

where g is the acceleration due to gravity and is $9.81 m/s^2$

If gb is positive, the rope is positively buoyant and floats due to a greater buoyancy force than gravity. If gb is negative, the rope is negatively buoyant and sinks due to a greater gravity force than buoyancy force.

3.0.4 Equations of Motion of the Rope

Newton's second Law states that the acceleration of the rope is the total force of the rope divided by the mass of the rope. Because the masses of the rope segments are concentrated in the nodes, all the rope forces that were calculated in the links should be converted from link forces to nodal forces. A necessary conversion to permit the application of Newton's second law. Additionally, the forces on the nodes at the ends that connect to the two

AUVs excluded from the equations of motion because these nodes do not possess any mass, as earlier mentioned. The internal and external forces acting on the rope segments are summed to determine the total force of each rope segment. The total force acting on the nodes is dictated in equation (3.32).

$$F_x^k = D_x^k + T_{a_x}^k + M_x^k \qquad F_y^k = D_y^k + T_{a_y}^k + M_y^k \tag{3.32}$$

The acceleration of the rope at each segment can be determined by dividing the total nodal forces by the mass of each rope segment.

$$\ddot{x}_{n^k} = \frac{F_x^k}{m_l} \qquad \ddot{y}_{n^k} = \frac{F_y^k}{m_l} \tag{3.33}$$

where $\ddot{x}_{l^j}$ and $\ddot{y}_{l^j}$ are the x and y components of the link acceleration

Rope Forces acting on the AUVs

The tug force from the towing AUV acting on the rope is equal to the summation of the forces acting on the first link of the rope. This rope forces from the first link acts opposite to the direction of the tug force from the towing AUV

$$F_{x_m} = -(T_{a_x}^{k=1} + D_x^{k=1}) \qquad F_{y_m} = -(T_{a_y}^{k=1} + D_y^{k=1}) \tag{3.34}$$

where F_{x_m} and F_{y_m} are the x and y forces of the towing AUV respectively

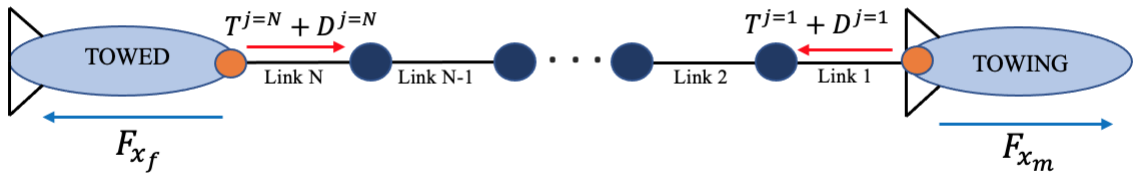

FIGURE 3.6: Tension Forces on ends of the rope.

The towed AUV on the other hand possesses a tug force acting on the rope which is equivalent to the total rope forces acting on the last link N.

$$F_{x_f} = T_{a_x}^{k=N} + D_x^{k=N} \qquad F_{y_f} = T_{a_y}^{k=N} + D_y^{k=N} \tag{3.35}$$

where F_{x_f} and F_{y_f} are the x and y forces of the towed AUV respectively

The forces from the ends of the rope create an induced moment on the AUVs. The induced moment is a function of the point of connection of the rope on the vehicle. l_{arm}, as previously stated represents the distance of the connection from CB. The sign of the l_{arm} changes based on if the rope is connected forward or aft of CB. When the rope is connected at CB, l_{arm} is 0 and there is no induced moment. The formulation for the induced moment acting on the AUVs is detailed in equation (3.36)

$$M_m = F_{y_m} \cdot l_{arm_m} \qquad M_f = F_{y_f} \cdot l_{arm_f} \tag{3.36}$$

where M_m and M_f are the induced moment from the rope acting on the towing vehicle and the towed vehicle respectively.

Chapter 4

Overall System Dynamics

The complete AUV-Rope system is a multi-body system, partitioned into individual sub systems for each AUV and the rope. The system is studied in a loosely coupled fashion in which the dynamics of each component is solved for using the inputs from the other sub systems at each time step. For the purpose of this work, the AUV-Rope System follows the outline of a towing AUV using a rope positioned aft, to tow another AUV. The initial conditions which include the position and velocity of each vehicle and the rope in the IRF must be specified. Additionally, the point of attachment of the rope on each AUV must be specified. The towing vehicle must be assigned a thrust while the towed AUV is designed to be propelled solely by the towing vehicle and does not utilize any thrust from the propellers.

In the framework of the system, there are provisions to specify the initial surge (u), sway (v) and yaw (r) velocities of the towing and towed AUVs in the program. These velocities can then be converted to IRF, using equations (4.1)

$$\dot{x}_0 = u_0 \cdot \cos\psi + v_0 \cdot \sin\psi_0, \quad \dot{y}_0 = v_0 \cdot \cos\psi_0 - u_0 \cdot \sin\psi_0, \quad \dot{\psi}_0 = r_0 \tag{4.1}$$

where $\dot{x}_0$, $\dot{y}_0$, ψ and $\dot{\psi}_0$ are the initial x, y, Euler angle for the horizontal plane (yaw) and angular velocity of the AUVs respectively. u_0, v_0 and r_0 are the initial surge, sway and yaw velocities of the AUVs respectively.

The initial position of the towing AUV in the IRF, x_{0_m} and y_{0_m} represents the location of the center of buoyancy (C.B) of the vehicle. Similarly, the initial position of the towed vehicle, x_{0_f} and y_{0_f} is situated at its center of buoyancy. The starting positions for the towed vehicle can be deduced from x_{0_m} and y_{0_m} with the rope length, L_r, the lever arm of both vehicles, l_{arm}, the initial yaw angular offset ψ, of the AUVs and the rope. In the framework, these variables are utilized to determine the attachment point of the rope on the towing vehicle, xp_0^m and yp_0^m. The initial location of the center of buoyancy of the towed vehicle becomes a function of xp_0^m and yp_0^m and can determined by following equation (4.2)

$$xp_0^m = x_{0_m} - l_{arm_m} \cdot \cos\psi_0^m \qquad yp_0^m = y_{0_m} - l_{arm_m} \cdot \sin\psi_0^m \tag{4.2}$$

Additionally, xp_0^m and yp_0^m as well as the initial rope angle can be utilized to determine the initial point of attachment of the rope on the towed AUV, xp_0^f and yp_0^f as shown in equation (4.3).

$$xp_0^f = xp_0^m - L_r \cdot \cos\psi_0^r \qquad yp_0^f = yp_0^m - L_r \cdot \sin\psi_0^r \tag{4.3}$$

The initial rope angle is a component of the rope position which specified ahead of the simulation. In the horizontal plane, the rope is assigned to be 0° to demonstrate all components of the system begin in a straight, level horizontal configuration. When the motion is rotated to the vertical plane, the rope angle may be specified to the desired angle needed. In this work, an angle of 90° is employed to showcase a straight vertical rope configuration. Finally, the starting positions of the towed AUV can be deduced from its rope point of attachment as detailed in equation (4.4)

$$x_{0_f} = xp_0^f - l_{arm_f} \cdot \cos\psi_{0_f} \qquad y_{0_f} = yp_0^f - l_{arm_f} \cdot \sin\psi_{0_f} \tag{4.4}$$

4.0.1 Program Flow Chart

Because the dynamics of the system are solved in loosely coupled fashion, the system is sensitive to the order in which the sub systems operate. The sub systems include the towing AUV, the rope and the towed AUV and chapters 2 and 3 discuss how they are respectively modeled. These sub systems require a main system where their inputs are integrated. The flowcharts describe in detail all the processes in both the sub code and the main program and can be useful manuals for properly understanding the framework.

AUV Sub-system

The initial conditions of the AUVs are contained in the main system and are only exported to the AUV subsystem on the first time step. For every time step, the AUV sub systems import the instantaneous BRF velocities (u, v), the angular rate r, as well as the angle of the vehicle, ψ from the main system. Additionally, the instantaneous tug forces of the respective vehicles, (F_{x_m}, F_{y_m}) and (F_{x_f}, F_{y_f}), thrust and rudder angle, δ_r are imported from the main system. Utilizing these values, the kinematics of the AUV is updated for the given time step within the AUV sub code. The updated instantaneous velocity and angular rate of the vehicles in IRF, $(\dot{x}, \dot{y})$ and $\dot{\psi}$ respectively and acceleration of the AUVs in the BRF $(\dot{u}, \dot{v}, \dot{r})$ are the final results of the AUV sub systems at the end of each time

step. These results are exported to the main system where the whole AUV-Rope System dynamics are solved. Within the main system, the results of the AUV subsystems for a given time step are processed to prepare the AUV subsystem imports for the next time step. The flowchart for the AUVs sub system is detailed in figure 4.1

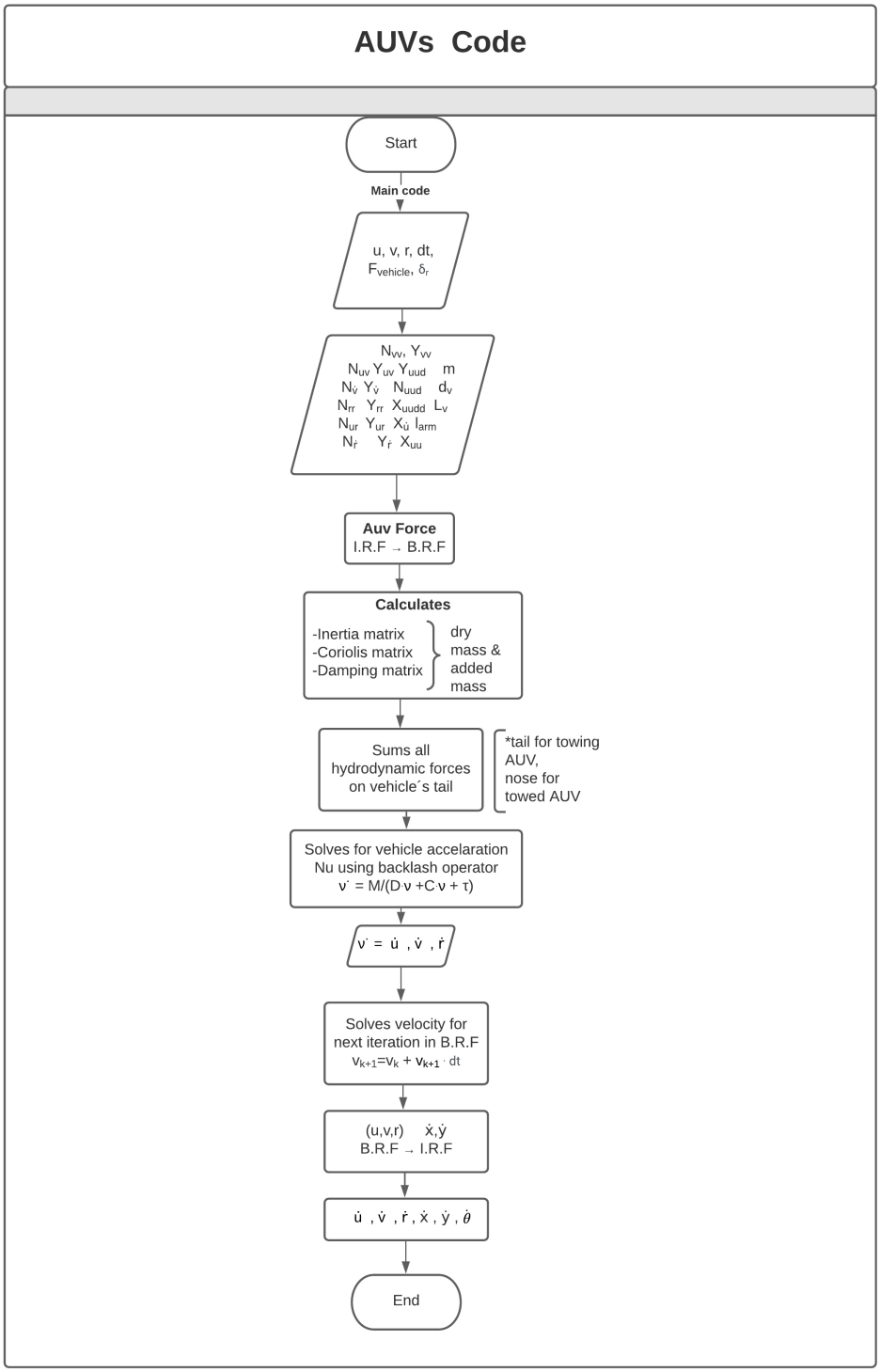

FIGURE 4.1: Flowchart describing the sub system for the towing and towed AUVs

Rope Sub-system

Similarly to the AUV subsystem, the states of the rope are imported from the main system for a given time step. These include the position and velocity of each node in IRF, the length of the rope (L_r), the mass of each segment (m_l) and the number of nodes N in the rope . Furthermore, the position and velocity of the attachment point of the rope on the towing AUV and the towed AUV, (xp_0^m, yp_0^m) and (xp_0^f, yp_0^f) respectively are imported from the main system. With knowledge of these inputs, the dynamics of the rope and its interactions with the vehicles can be studied to determine the updated acceleration of the links in IRF (x_{lj}, y_{lj}) and the updated tug forces on the rope ends from each of the AUVs, (F_{x_m}, F_{y_m}) and (F_{x_f}, F_{y_f}). The final results of the given time step are exported to the main system for further analysis. This process is repeated for every time step and is shown in the flowchart in figure 4.2

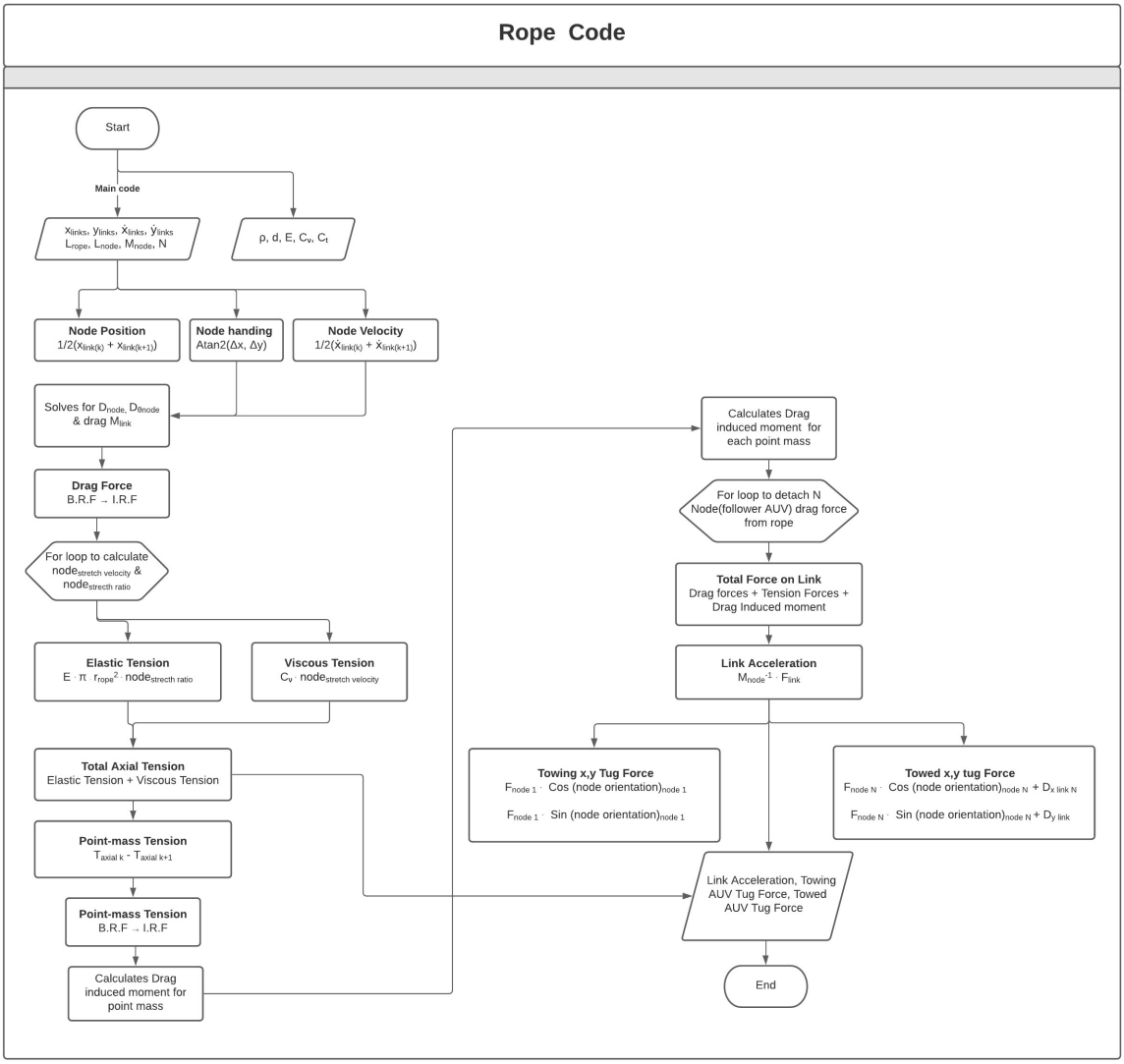

FIGURE 4.2: Flowchart demonstrating the order of processes in the Rope Sub system

Main System

The main system is a framework that integrates all the sub components of the system, and solves the complete AUV-Rope dynamics. The initial conditions of both AUVs and the rope are specified in the main system. Utilizing the initial position and velocities of the sub components, the necessary variables for each sub system is determined. The sub systems utilize these inputs and yield the acceleration of the AUVs and rope as well as the tug forces on the rope. The acceleration of the rope and AUVs are used to derive their respective velocities and positions for the next time step. The process is repeated until the final time of the simulation is reached. The flow chart for the main system framework can be seen in figure 4.3

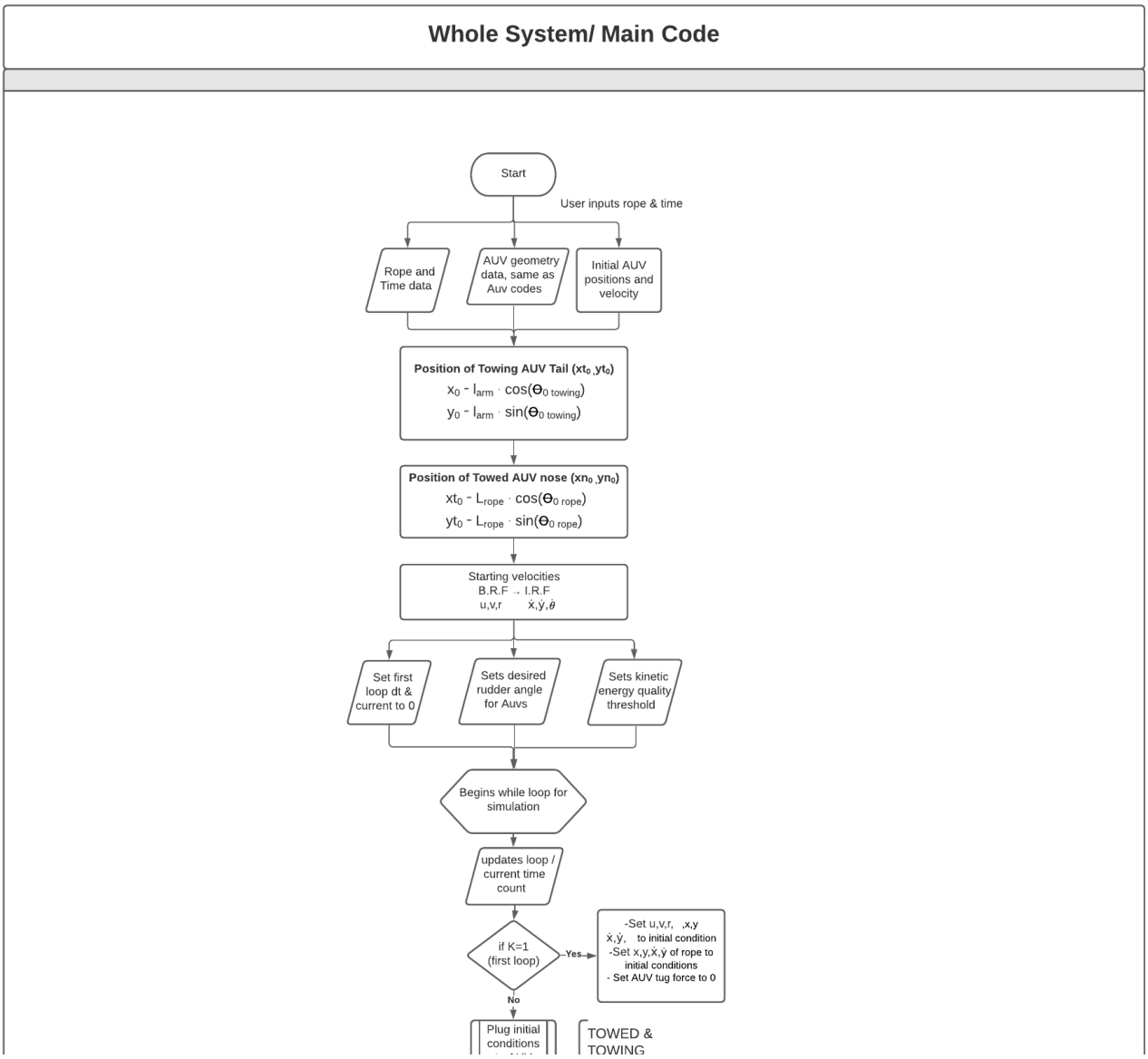

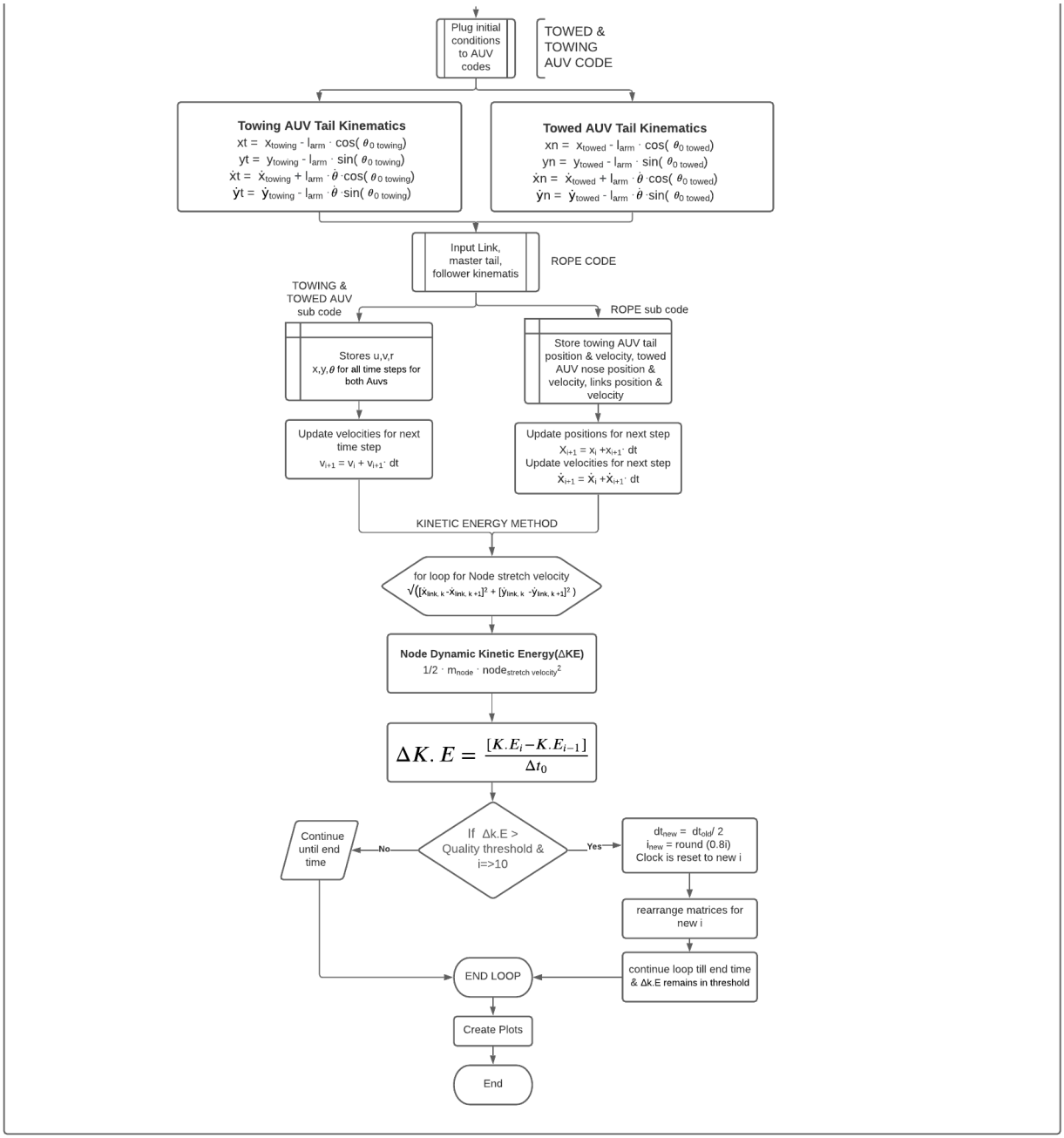

FIGURE 4.3: Flowchart detailing the Main System Framework

4.0.2 Motion of the Rope Point of Attachment on the AUV

The position and velocity of the AUVs for the next time step are derived using forward Euler approximation with the acceleration of the AUV at the given time step. This is outlined in equation (4.5). Before the update occurs, the position and velocity values of the current time step are stored to enable plotting the system's trajectory. Forward euler is an approximation technique and its accuracy is dependent on the chosen time step, dt. The solution becomes more accurate as dt becomes smaller. Unfortunately, reducing dt significantly increases the computation time and cost of the simulation.

$$x_{i+1} = x_i + \dot{x}_i \cdot dt \qquad y_{i+1} = y_i + \dot{y}_i \cdot dt \qquad \theta_{i+1} = \theta_i + \dot{\theta}_i \cdot dt \tag{4.5}$$

where i is iteration number

Similarly, the BRF velocities for the next time step can be computed using forward euler approximation as shown in equation (4.6).

$$u_{i+1} = u_i + \dot{u}_i \cdot dt \qquad v_{i+1} = v_i + \dot{v}_i \cdot dt \qquad r_{i+1} = r_i + \dot{r}_i \cdot dt \tag{4.6}$$

The position and velocity of the AUVs are calculated at the C.B of the vehicle. The position and velocity of the towing vehicle at the rope attachment point can be deduced using the lever arm of the vehicle, l_{arm}. This is denoted by equation (4.7). Here, xp^m and yp^m are dependent on the sign of the lever arm and whether the rope is attached forward or aft of C.B. When attached forward of C.B, l_{arm} is negative and when aft of C.B, the lever arm becomes positive.

$$xp^m = x_m \pm l_{arm_m} \cdot \cos\theta_m \qquad yp^m = y_m \pm l_{arm_m} \cdot \sin\theta_m \tag{4.7}$$

where xp^m and yp^m are the x and y positions of rope attachment on the towing AUV respectively.

The velocity of the towing AUV at the attachment point is given by

$$\dot{xp}^m = \dot{x}_m \pm l_{arm^m} \cdot \dot{\theta}_m \cdot \sin\theta_m \qquad \dot{yp}^m = \dot{y}_m \pm l_{arm^m} \cdot \dot{\theta}_m \cdot \cos\theta_m \tag{4.8}$$

where $\dot{xp}^m$ and $\dot{yp}^m$ are the x and y velocity of the towing AUV. respectively.

The position and velocity of the rope attachment point on the towed AUV are calculated similarly to the towing vehicle as shown in (4.9) and (4.10).

$$xp^f = x_f \pm l_{arm^f} \cdot \cos\theta_f \qquad yp^f = y_f \pm l_{arm^f} \cdot \sin\theta_f \tag{4.9}$$

where xp^f and yp^f are the x and y positions of rope attachment on the towed AUV respectively.

$$\dot{xp}^f = \dot{x}_f \pm l_{arm^f} \cdot \dot{\theta}_f \cdot \sin\theta_f \qquad \dot{yp}^f = \dot{y}_f \pm l_{arm^f} \cdot \dot{\theta}_f \cdot \cos\theta_f \tag{4.10}$$

where $\dot{xp}^f$ and $\dot{yp}^f$ are the x and y velocity of the towed AUV respectively.

4.0.3 Numerical Stability Improvement Methods

Flexible marine cables present difficulties when modeling due to their non linear nature. A drawback of the modeling method employed in this work, is the potential for discontinuities and presence of noise. A rope may withstand tension but not compression. Likewise, LMSD performs excellently in modeling the rope under tension but declines under compression [19]. These difficulties are highlighted during motions that forced the rope to compress. The compressive motions are referred to as pinching motions in the rest of this chapter.

Pinch Motion Correction of Rope Segments

This pinching motion typically occurs when some nodes of the rope begin to veer off the average direction of the rope causing the rope segments to compress and graze each other. An example of this scenario is detailed in figure 4.4. This compression creates a significant amount of vibration in the rope, which can grow and cause further compression until the whole system fails. A correction to this pinching motion involves setting a max sway value on the nodes, which once exceeded, the node correction begins and sets the defaulting nodes back in the correct path. This modification can be achieved by utilizing the velocities of the surrounding nodes to approximate the correct velocity of the swaying node. This requires the node velocities to be analyzed along the correct vector path. The vector path is defined as the direction perpendicular to the line between any three 3 surrounding nodes, $j-1$, j , $j+1$. The normal vector is given by

$$\begin{bmatrix} nv_x \\ nv_y \end{bmatrix} = \begin{bmatrix} \frac{x_l(j)-x_l(j-1)}{\sqrt{[x_l(j)-x_l(j-1)]^2+[y_l(j)-y_l(j-1)]^2}} \\ \frac{y_l(j)-y_l(j-1)}{\sqrt{[x_l(j)-x_l(j-1)]^2+[y_l(j)-y_l(j-1)]^2}} \end{bmatrix} \tag{4.11}$$

where nv_x and nv_y are the x and y components of the normal vector

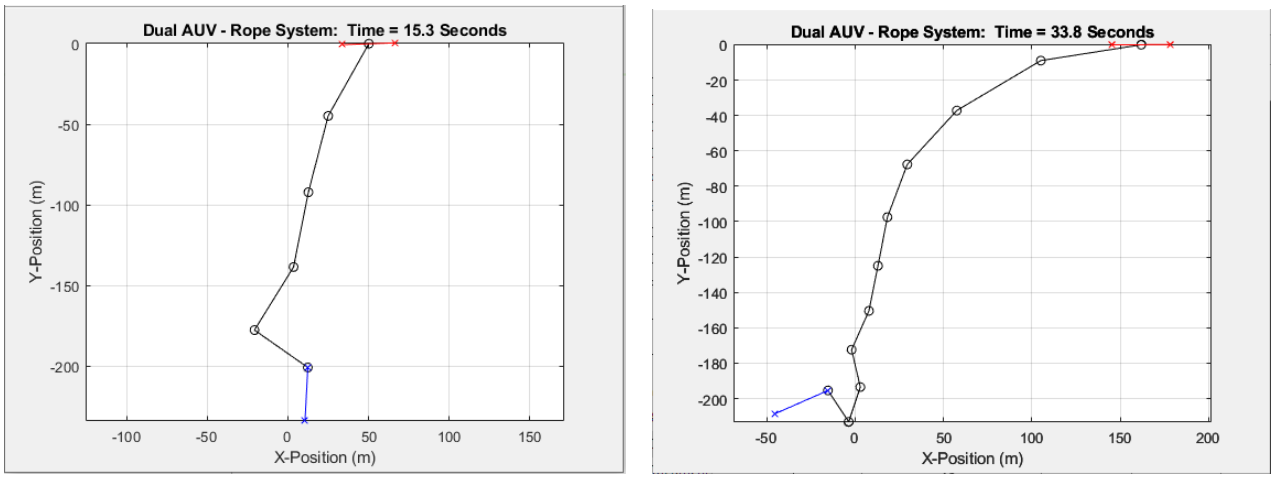

FIGURE 4.4: Illustration of potential pinching motion during simulation

The velocity along that normal vector path for each of the 3 surrounding nodes is calculated to enable their comparison.

$$V_n^{j-1} = \begin{bmatrix} \dot{x}_l^{j-1} \\ \dot{y}_l^{j-1} \end{bmatrix} \cdot \begin{bmatrix} nv_x \\ nv_y \end{bmatrix} \tag{4.12}$$

$$V_n^{j} = \begin{bmatrix} \dot{x}_l^{j} \\ \dot{y}_l^{j} \end{bmatrix} \cdot \begin{bmatrix} nv_x \\ nv_y \end{bmatrix} \tag{4.13}$$

$$V_n^{j+1} = \begin{bmatrix} \dot{x}_l^{j+1} \\ \dot{y}_l^{j+1} \end{bmatrix} \cdot \begin{bmatrix} nv_x \\ nv_y \end{bmatrix} \tag{4.14}$$

where $V_n(j)$ is the normalized vector at node j

The sway difference value, s_d in this case is assigned to be $1m/s$ but can always be specified to appropriately match another scenario where the segments experience higher or lower pinching motions. Based on s_d, a criteria for activating the node correction is set and is shown in equation (4.15)

$$|V_n^{j-1} - V_n^{j}| > s_d < |V_n^{j} - V_n^{j+1}| \tag{4.15}$$

The velocity of the defaulting rope segment $\dot{x}_l^j$, $\dot{y}_l^j$ is approximated by assuming the despite uneven stretching across the rope, neighbouring links are of equal length and their nodes are spaced apart equally. This assumption is made because the rope segments are small due to the high number of nodes chosen. At lower total number of node values, this assumption may not be valid. Utilizing this assumption, the velocity of defaulting segment j should be half of the sum of $j-1$ and $j+1$.

$$\dot{x}_{l\,c}^{j} = \frac{\dot{x}_l^{j-1} + \dot{x}_l^{j+1}}{2}, \qquad \dot{y}_{l\,c}^{j} = \frac{\dot{y}_l^{j-1} + \dot{y}_l^{j+1}}{2} \tag{4.16}$$

where $\dot{x}_{l\,c}^{j}$ and $\dot{y}_{l\,c}^{j}$ are the corrected link velocities of link j

Improving Accuracy of Forward Euler Approximation

Another potential area where noise may affect the results of the simulation is the value of the time step, dt. Forward euler approximation is used across the rope to solve for the motion of the rope and approximate its position and velocity. When dt is large, it saves a significant amount of computation time and cost but a lot of vibration becomes present. The vibration becomes compounded because these values are inputs to other values and

the inaccuracy due to the approximation continues growing. The inaccuracy is significantly highlighted when the vehicles begin to tug the rope. We incorporated a method to check this vibration to ensure it never exceeds a certain value. This was achieved by monitoring the kinetic energy, Ke of the rope, since it behaves like a spring. The Kinetic Energy of the rope at each time step is calculated using the mass of the segment, m_l and the sum of the link stretch velocity of all of the links, l_{SV}

$$Ke_i = \frac{M_n \cdot \sum_{k=1}^{k=N} {l_{SV}}^2}{2} \tag{4.17}$$

A quality threshold value, q_t is assigned. When the difference between the kinetic energy of the rope of the previous time step, $i-1$ and the current iteration i is equal or greater than q_t, dt is halved. The condition for halving is denoted by equation (4.18)

$$\Delta Ke \geq q_t, \quad \Delta Ke = \frac{[Ke_i - Ke_{i-1}]}{dt} \tag{4.18}$$

where ΔKe is the difference in the kinetic energy of the iterations, Ke_i is the kinetic energy of the rope at iteration, i and dt_0 is the current time step

Once dt is halved, the new time step dt_n is given by equation (4.19). The simulation repeats previous iterations with the new time step to prepare better results with less vibration present. Current time of the simulation, t_c is reduced by 20% and rounded to the nearest integer around that value. This is achieved with the "round" function in MATLAB as denoted in equation (4.20).

$$_n = \frac{dt}{2} \tag{4.19}$$

$$t_n = round(0.8 \cdot t_c) \tag{4.20}$$

where t_n is the new current time for the simulation

4.0.4 Catenary Shape Analysis of the Rope System

The catenary of a cable details the shape of a flexible cable hanging from its ends. The equation for the catenary of a cable was identified by Gottfried Leibniz, Christiaan Huygens, and Johann Bernoulli in the 16th century. Its applications are vast and include construction of archs and suspension bridges, as well as mooring systems for ships. Leibniz

et al developed the equation for the catenary shape of a rope which is given by equation (4.21) [20][21].

$$z(x) = a \cdot \left(\frac{e^{\frac{x}{a}} + e^{\frac{-x}{a}}}{2} \right) \Rightarrow z(x) = a \cdot cosh\left(\frac{x}{a}\right) \tag{4.21}$$

where x and z are the x and z positions of the curve respectively and a is the sag parameter of the rope

The catenary shape of the rope system is assessed using a 50m rope and two AUVs. Here, the towing AUV is fixed in a static position and does not surge, heave or pitch. The initial depth of the rope is at the free surface and the rope can move freely in all degrees of freedom. Under action of all the forces acting on the rope, the rope sinks until it approaches its steady state position as depicted in figure 4.5. The maximum deflection of the rope is dependent on different factors such as the length of the rope, the tension in the rope and the material of the rope. The maximum deflection of the rope can be altered with modifications to these parameters.

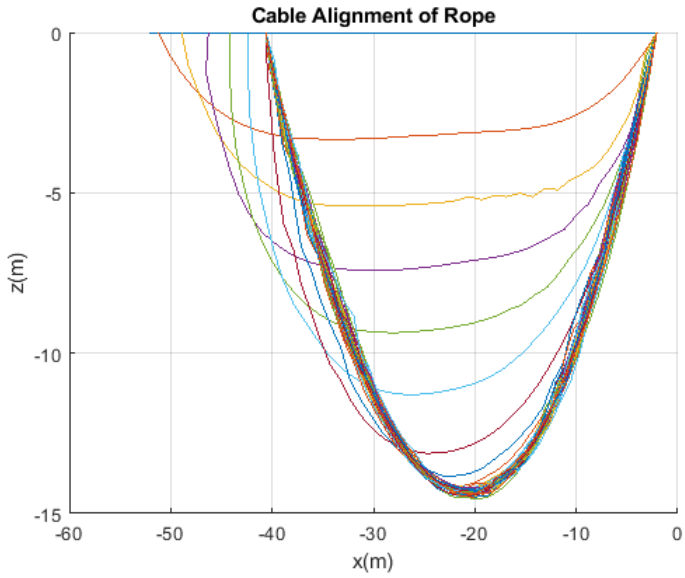

FIGURE 4.5: Time history of the cable alignment during test

The maximum deflection of the rope occurs around 15m as denoted in figure 4.6. Utilizing the position of the ends of the ropes and the maximum deflection point, the catenary equation of the rope can be determined. The traditional catenary equation in equation (4.21) must be modified to account for this rope not being centered around point(0,0). This modification requires the use of the x and z vertex points which are symbolized by x_c and z_c in equation (4.22).

$$z(x) = z(x) + z_c = a \cdot cosh\left(\frac{x + x_c}{a}\right) \tag{4.22}$$

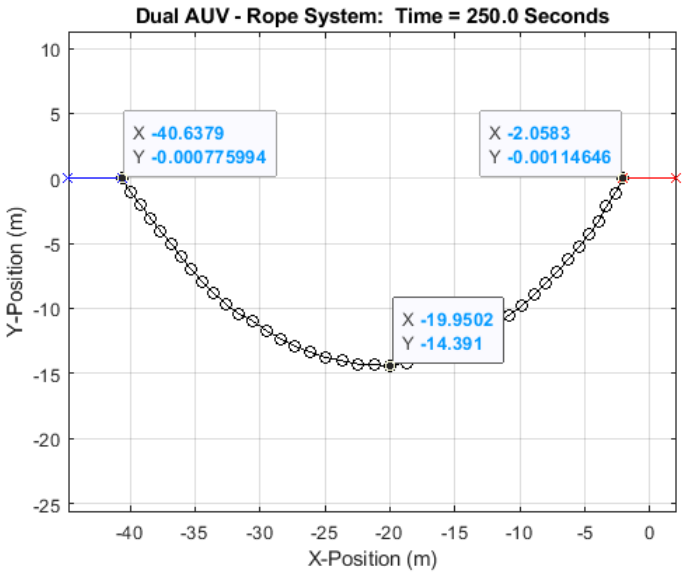

FIGURE 4.6: Steady state position of rope

Using curve fitting tools, the x and z vertices of the rope can be determined. Additionally, the sag parameter of the rope can be deduced with knowledge of the vertex of the curve. Equation (4.23) details the catenary equation for the rope system in its steady state.

$$z(x) + 29.2587 = 14.7821 \cdot cosh\left(\frac{x + 21.3481}{14.7821}\right) \tag{4.23}$$

The cable alignment in the steady state of the rope system is compared to the catenary equation curve for the rope as denoted in figure 4.7. Both curves depict good agreement between the catenary equation and rope system while posing some differences. The catenary curve equation is symmetric and bears no contours. Alternatively, the rope is asymmetric and presents contours. This is due to the dynamic nature of the rope. Additionally, as discussed in previous sections, the rope utilizes approximations and its spring damper nature causes the rope to vibrate. Corrective measures are implemented to reduce these concerns in more dynamic conditions. In static cases like this, the corrective measures appear to be less effective and may require more computational cost to bring the rope alignment closer to the catenary curve.

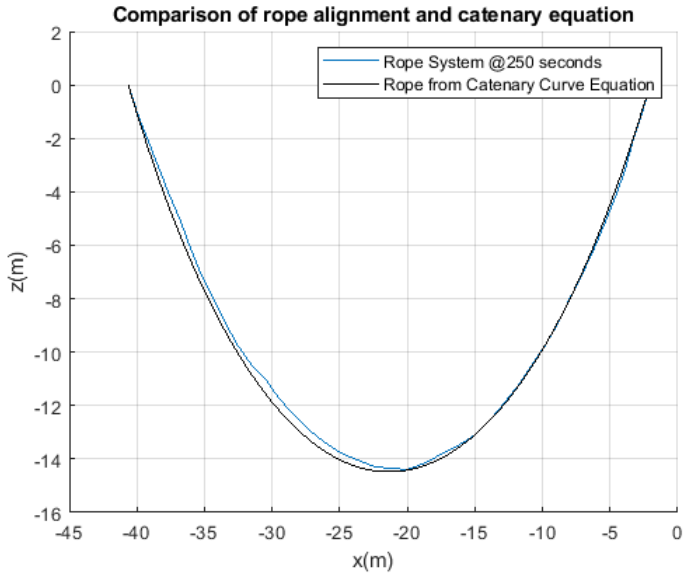

FIGURE 4.7: Comparison of cable alignment of rope and catenary curve of the rope

However, this static test highlights that the rope system behaves in a catenary fashion and the framework is robust and performs as expected even in more extreme conditions like this static case.

Chapter 5

Assessment of Maneuverability of AUV-Rope Towing System

Maneuverability is defined as the ability of a vehicle to change its course. In this chapter, we investigate the maneuverability of the AUV-Rope system following conventional evaluation methodologies from the International Maritime Organisation. IMO developed standards to highlight critical qualities that a vessel must possess when its performance is evaluated. These qualities include the course keeping, the course changing and the turning abilities of the vehicle [22] .

The AUV-Rope towing system is assessed for maneuverability using three different cases. The first two motions are focused in the horizontal plane, where the rope is attached to the stern of the towing vehicle and the bow of the towed vehicle. In the first case, a straight line test is performed and the towing vehicle tows the towed vehicle from rest without any rudder deflection to initiate turning. In the second case, the AUV-Rope system begins from rest and a zigzag maneuver is initiated once full speed is achieved. The AUV-Rope system employs the rudder of the towing vehicle to introduce the turning motion on the system.

The third case involves motion in the vertical plane. Here, the towing vehicle travels around the free surface whilst the towed vehicle is submerged 200m underwater [23].

The hydrodynamic coefficients of the AUVs for each of these cases mentioned are approximated using analytic and semi-empirical (ASE) methods from Kepler [9]. Kepler developed the model for deriving coefficients following findings from [24][12][25][26][27]. Employing Kepler's model, coefficients for symmetrical prolate spheroid hulled AUVs can be easily determined.

5.0.1 Case 1: Pure Surge Accelerated Motion

The towing and towed vehicle are both modeled after the Virginia Tech 690 with a scale factor of 2 used to scale the length and diameter of the 690. The increase in the dimensions from the original 690 similarly leads to an increase in the mass to become 282kg. A 50m polyester rope with 20 nodes is featured in this test. The rope is attached at the CB for both the towing vehicle and the towed vehicle. The complete parameters of the AUV-Rope system for this case appear in table 5.1.

Parameter	Value	Unit
Length of vehicle (l_v)	4.1148	m
Diameter of vehicle (d_v)	0.3505	m
Vehicle Mass (m)	282.1261	kg
x_p of Towing Vehicle	$-\frac{lv}{2}$	m
x_p of Towed Vehicle	$+\frac{lv}{2}$	m
Rope Length (L_r)	50	m
Rope Mass (M_r)	16.2170	kg
Rope Diameter (D_r)	0.024	m
Young's Modulus of Rope (E)	$2.08 \cdot 10^6$	$kg/(m \cdot s^2)$
C_t of Rope	0.00739	N/A
C_v of Rope	0.05	kg/s

TABLE 5.1: Vehicle and Rope Parameters

The duration of the simulation is 150 seconds with a desired surge velocity of 2m/s. To estimate the minimum required thrust to reach the desired surge velocity, the formulations by Njaka in [28] are followed. Njaka found that the thrust must be greater than the drag acting on the vehicles at the desired velocity. The drag force of each vehicle is expressed by equation (5.1) and is determined using the surge based hydrodynamic coefficient, X_{uu} .

$$F_D = X_{uu} \cdot u \tag{5.1}$$

where F_D is the drag force on a vehicle at a given velocity

Because the towing system involves the towing vehicle, the towed vehicle, as well as a rope, the drag of both vehicles are combined to determine the minimum thrust required to achieve the desired surge velocity. The minimum required thrust is denoted in equation (5.2).

$$F_T \geq F_D^m + F_D^f \tag{5.2}$$

where F_D^m and F_D^f are the drag force on the towing and towed vehicle respectively

The test evaluates the course keeping ability of the AUV-Rope system and assesses how effectively the system accelerates from rest. Both vehicles are assigned a 0 ° heading angle, since it is a straight line test. Furthermore, both vehicles maintain a 0 ° rudder angle for the entirety of the simulation. Figure 5.1 depicts the surge velocities of both vehicles when a thrust force of 63 N is assigned to the towing vehicle. The desired surge velocity of 2 m/s is initially achieved by the towing vehicle around 40 seconds into the simulation. After which, the towed vehicle reaches 2m/s around 50 seconds. Highlighting a time lag between the surge velocities of both vehicles. Both vehicles maintain their course and do not experience significant yaw and sway motions.

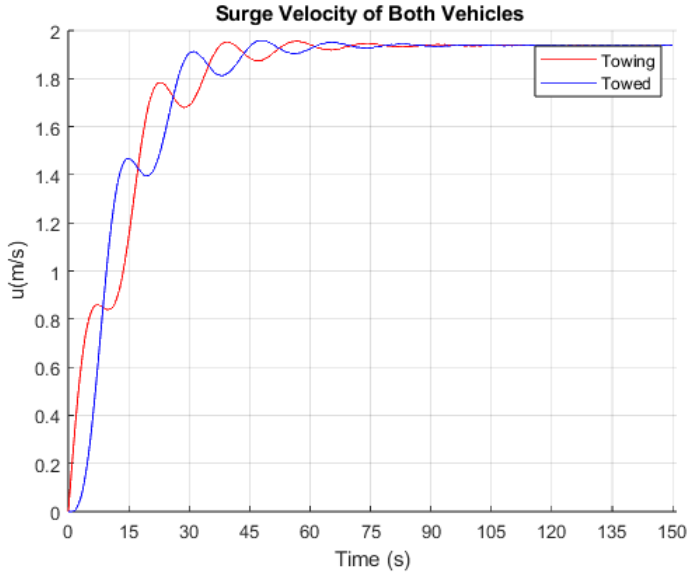

FIGURE 5.1: The surge velocity, u of the towing and towed vehicle.

The maneuver is dominated by surge motion, creating tug forces on the rope in the X direction which are equal and opposite in direction. The tug forces which represent the total forces of the rope acting on the vehicle, are greatest in magnitude right after the system accelerates from rest. Once the system reaches the desired surge speed, acceleration is minimal and the tug forces remain relatively constant. The time history of the tug forces for both the towing and towed vehicle are depicted in figure 5.2 .

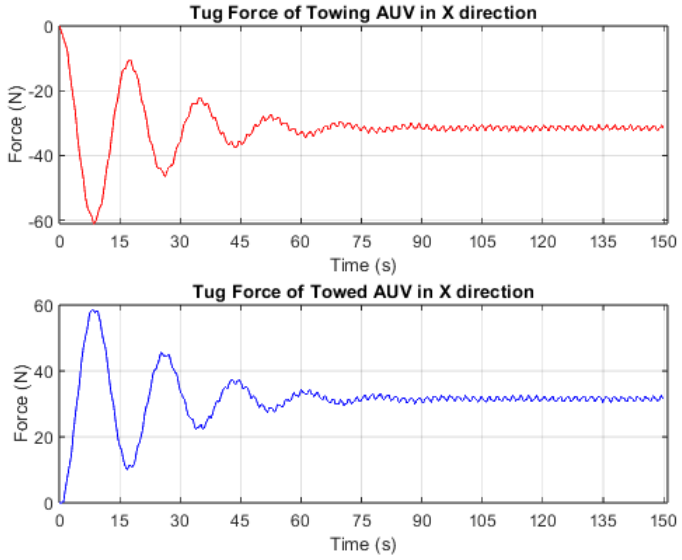

FIGURE 5.2: The tug force of the towing vehicle (Top) and the towed vehicle (Bottom) at 2m/s

5.0.2 Case 2: 10°/10° Zigzag Maneuver in the Horizontal Plane

The zigzag maneuver assesses the yaw response and course changing performance of a vehicle. In a zigzag maneuver, the rudder angle is prescribed to a fixed angle until the vehicle reaches a given yaw angle, then the rudder angle is prescribed to the opposite angle until the vehicle achieves the given yaw angle in the opposite direction. The alternation of the rudder angle continues until the maneuver is completed. In this case, a 10/10 zigzag maneuver was performed. Thus, the given rudder angle is 10 °. The performance of the maneuver is evaluated using the overshoot angle according to the requirements of the IMO in [29]. The overshoot angle is the difference between the prescribed rudder angle and the vehicle heading. The AUV-Rope system must meet the criteria set by IMO for both the first overshoot and the second overshoot angles. The first overshoot angle of the towing vehicle must not exceed the values in equation (5.3) to be considered stable [29].

$$\textbf{1st Overshoot} \begin{cases} 10^\circ & l_v/u < 10 \\ 5 + 1/2(l_v/u)^\circ & 10 \geq l_v/u < 30 \\ 20^\circ & l_v/u \geq 30 \end{cases} \tag{5.3}$$

The second overshoot angle of the towing vehicle corresponds to the rudder command after the first. It must follow the criteria in equation (5.4)

$$\textbf{2nd Overshoot} \begin{cases} 25^\circ & l_v/u < 10 \\ 17.5 + 0.75(l_v/u)^\circ & 10 \geq l_v/u < 30 \\ 40^\circ & l_v/u \geq 30 \end{cases} \tag{5.4}$$

For this maneuver, the AUVs have the same characteristics as Case 1 as well as the same hydrodynamic coefficients. The rope also bears the same characteristics as in Case 1. The system begins with both AUVs at rest and 163 Newtons thrust is assigned to only the towing AUV. The rudder of the towing AUV is fixed at 0° for the first 25 seconds to allow the AUVs to reach the desired surge velocity. Once the desired surge velocity is achieved, the rudder is prescribed to 10° until the yaw angle approaches 10 °. After which, the rudder is alternated back and forth between -10° and 10° for the remainder of the motion.

The heading angle of both AUVs are depicted in figure 5.3. The illustration denotes that first and second overshoot of the towing AUV do not exceed the standards set for the maneuver throughout the duration of the simulation. The towed vehicle's heading appears to be minimally affected during this maneuver and remains around 0 due to the long rope employed as well as the nature of the maneuver. A 10°/10° maneuver does not feature a steep turn. Coupled with the length of the rope which could reduce the intensity of the turn, the yaw motion in the towed vehicle becomes minimal. The heading of the towing vehicle on the other hand, alternates periodically following the prescribed rudder angle, as expected.

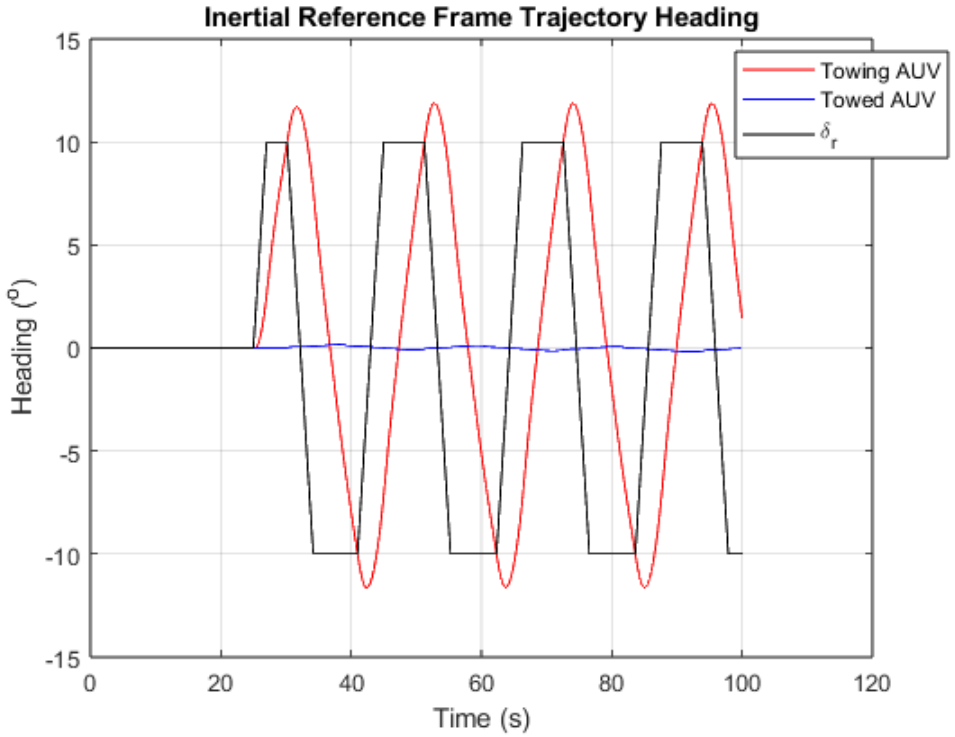

FIGURE 5.3: The prescribed rudder angle and vehicle heading of the towing and towed vehicle.

The surge velocity and the yaw rate of both vehicle are shown in figures 5.4a and 5.4b. Both vehicles achieve a surge velocity of about 3 m/s. The yaw rate of the towed vehicle remains negligible through out the motion and confirms its relatively small heading angle when compared to that of the towing vehicle.

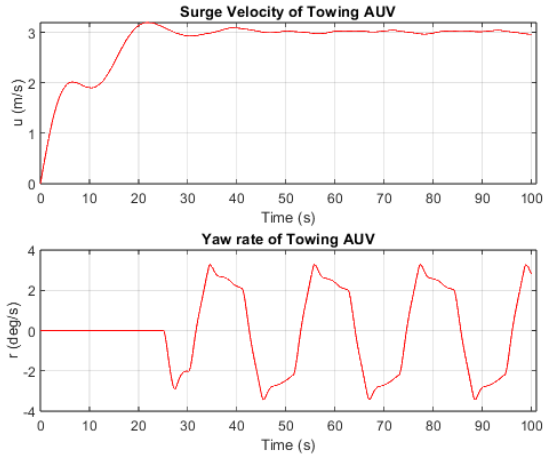

(A) The surge velocity and yaw rate of the towing vehicle

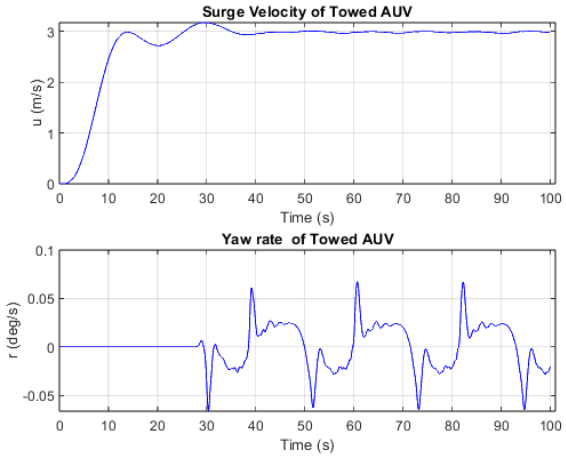

(B) The surge velocity and yaw rate of the towed vehicle

The trajectory of the vehicles in the horizontal plane can also be studied and compared with the tug forces both vehicles impact on the rope. The motion showcases the newton

pair tug forces in the x direction as depicted in figures 5.7a and 5.7b. Both vehicles travel together but the magnitude of their sway motions defer as illustrated in the trajectory of the system in figure 5.5 .

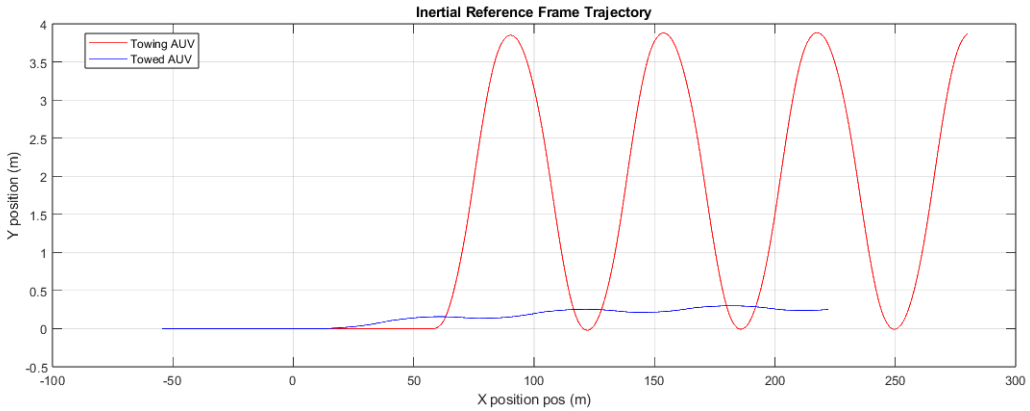

FIGURE 5.5: The trajectory of the towing and towed vehicle in the Horizontal Plane.

Additionally, the motion of the rope can be studied in detail as denoted in figure 5.6, where the trajectory of each node of the rope during the maneuver is displayed. Similarly to the towed vehicle, the nodes closest to the last node of the rope travel shorter distances when compared to the nodes closest to the towing vehicle.

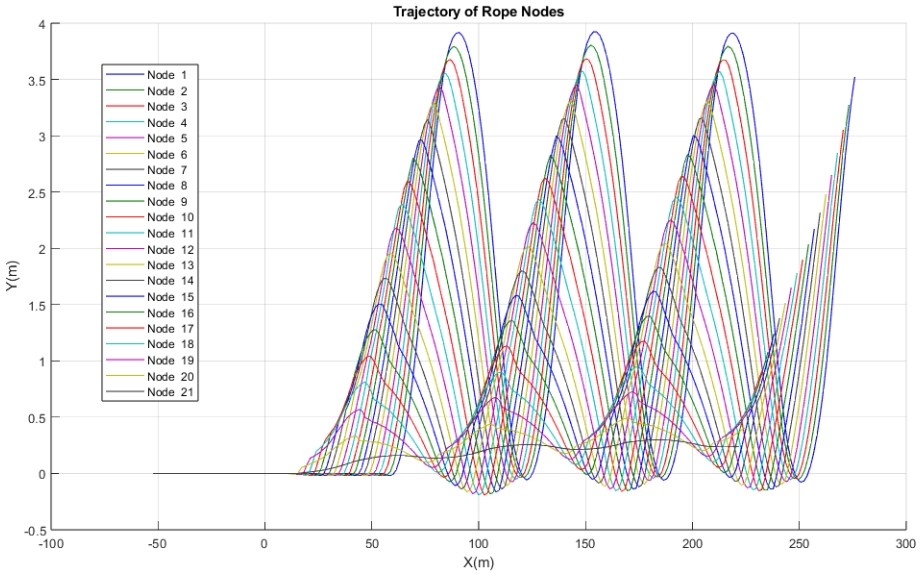

FIGURE 5.6: The trajectory of each node of the rope during zigzag maneuver.

Examining the yaw motion and trajectories of both vehicle, differences in the tug forces can be anticipated. Figures 5.7a and 5.7b depict a notable difference in the tug forces in

the y direction of both vehicles. Conversely in the x direction, both vehicles have equal and opposite tug forces because their surge velocities are equivalent.

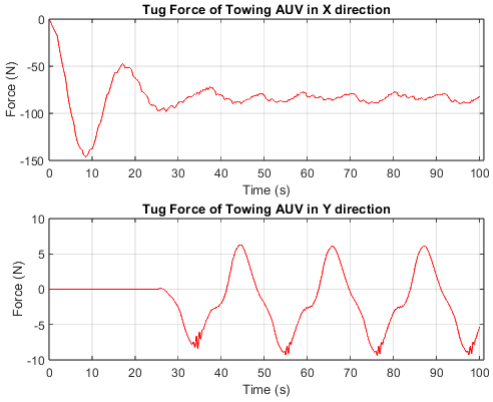

(A) The tug force of the towing vehicle on the rope

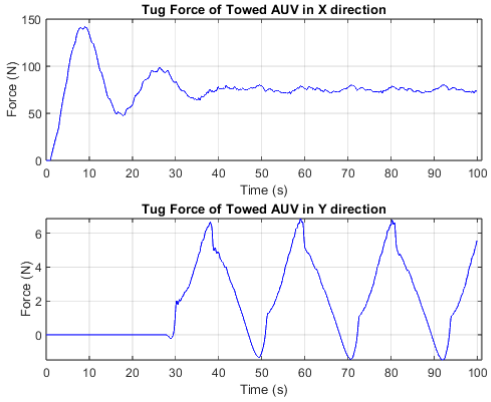

(B) The tug force of the towed vehicle on the rope

5.0.3 Case 3: Towing Maneuver in the Vertical Plane

Park and Kim in [23], explore the motion of a towing vehicle traveling around the water surface and a tow fish that is submerged 200 meters below the water surface. The towfish is not self propelled and is connected to the towing vehicle by a 200m long marine cable as shown in Figure 5.8. As depicted in the illustration, Park and Kim state that the rope is connected to the center of buoyancy of the towing vehicle and the bow of the towed vehicle.

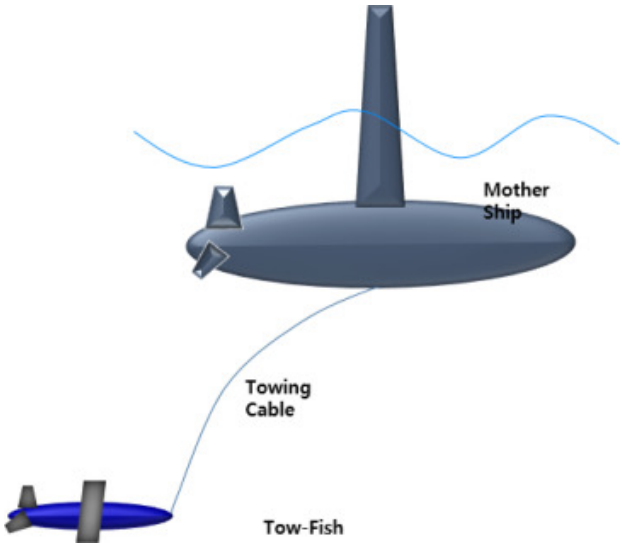

FIGURE 5.8: Illustration of the Towing System

The towing vehicle and the towfish are modeled after the Integrated Submergible for Intelligent Mission Implementation (ISimI). ISimI has a Myring hull profile and was developed

by the Korea Ocean Research and Development Institute (KORDI). The vehicle can be seen in Figure 5.9 and its hull parameters can be found in [1]

FIGURE 5.9: The ISimI vehicle from Maritime and Ocean Engineering Research Institute (MOERI) [1]

The towing vehicle has a significantly larger hull than the towed vehicle. The vehicles are scaled appropriately utilizing the hull parameters of ISimI and their principal dimensions are detailed in tables 5.2a and 5.2b. Furthermore, the towfish is designed to be a glider and utilizes the fin parameters from [30]. However, the position of the wing on the glider was not specified and had to be approximated based on figure 5.8 and the stability of the vehicle. The hydrodynamic coefficients of these vehicles are calculated using ASE methods and can be found in appendix A. The scaled profile of the towfish with the fins is shown in figure 5.10. Additionally, the heave velocity of the towing vehicle is fixed to minimize fluctuations in the depth of the towing vehicle.

Parameter	Value	Unit
l_v of Towing vehicle	8.3	m
d_v of Towing vehicle	1.1857	m
m of Towing Vehicle	6950	kg
x_p of Towing Vehicle	0(C.B)	m

(A) Towing Vehicle Parameters

Parameter	Value	Unit
l_v of Towed vehicle	3.3	m
d_v of Towed vehicle	0.4714	m
m of Towed Vehicle	416	kg
x_p of Towed Vehicle	Bow	N/A

(B) Towed Vehicles Parameters

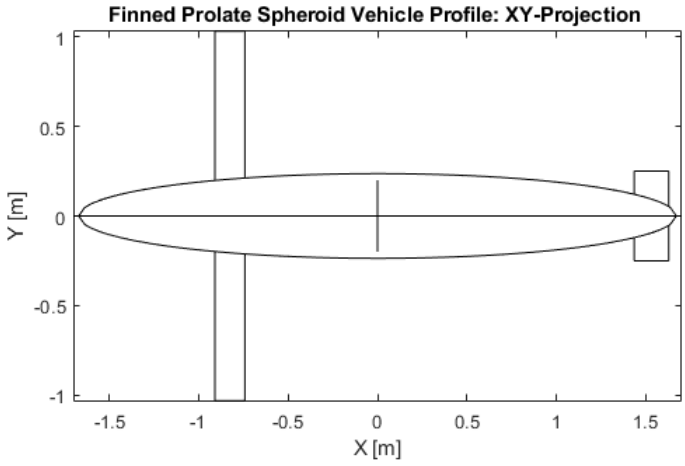

FIGURE 5.10: The scaled profile of the Towfish

The rope parameters are given in [23] but omits information about the viscous damping coefficient of the rope and the material of the rope used. These are important parameters that largely affect the results of the simulation. An approximation is made utilizing the density of the rope and the mass of the vehicles being towed. The given density of the rope is about that of steel and the vehicle being towed is heavy and requires a very strong rope. We assume the rope is made of steel and the complete characteristics for this rope are detailed in table 5.3

Parameter	Value	Unit
Rope Length (L_r)	200	m
Rope Mass (M_r)	338	kg
Rope Diameter (D_r)	0.024	m
Rope Density (ρ_r)	1300	kg/m^3
Young's Modulus of Rope (E)	$7 \cdot 10^8$	$kg/(m \cdot s^2)$
C_t of Rope (C_t)	0.00886	N/A
C_v of Rope	0.05	kg/s

TABLE 5.3: Rope Parameters

In this maneuver, the towed AUV is set to operate near 3.5 meters below the water surface. The focus of the maneuver is to study the dynamic interaction between the towed vehicle, the rope and the towing vehicle. The system is simulated for 100 seconds according to (Park and Kim, 2015) and figures 5.11a and 5.11b detail the surge, heave and pitch velocities during the maneuver. The AUV towing system accelerates from rest to the desired constant

forward speed of 6 m/s. The towing AUV achieves the desired surge velocity at around 70 seconds. The velocities of both vehicles highlight the interaction between the rope and the towed vehicle. The initial tug motion on the towed vehicle creates increased heave and pitch motions which stabilize once the constant forward speed is achieved.

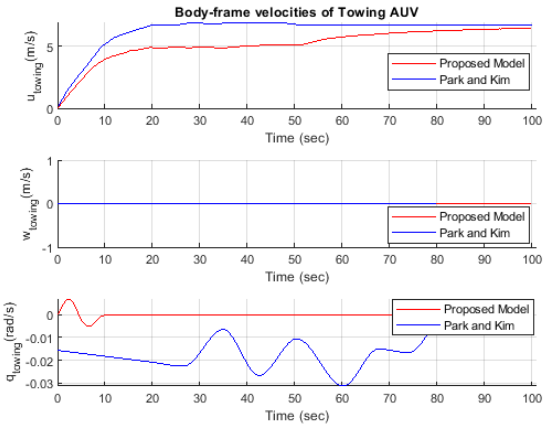

(A) The surge, heave and pitch velocities of the towing vehicle

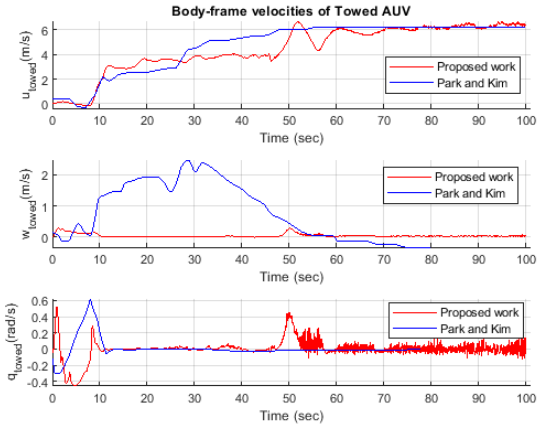

(B) The surge, heave and pitch velocities of the towed vehicle

The time history of the catenary of the rope is denoted in figure 5.12. When the AUV-towing system begins from rest due to the thrust from the towing vehicle, the catenary of the rope changes. With increasing forward speed of the towing vehicles, the degree of inclination in the catenary of the rope changes to a more horizontal alignment. The catenary is dictated by a number of factors including the relative density of the rope compared to water as well as the diameter and young's modulus of the rope [31]. Ropes with larger relative densities to water behave negatively buoyant while ropes with smaller relative densities to water are positively buoyant. Additionally, increase in the diameter of the rope increases the drag of the rope during motion, increasing the tendency of the rope sinking.

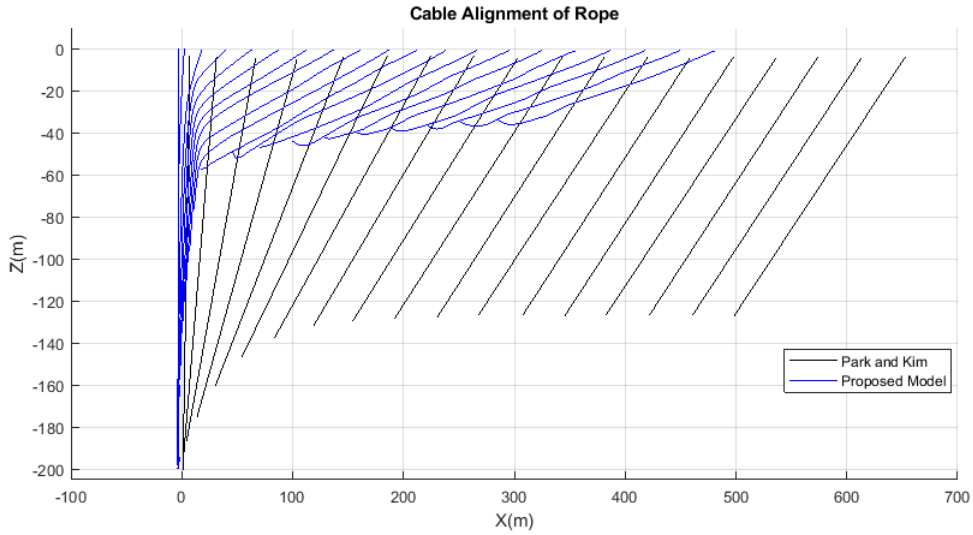

FIGURE 5.12: The cable alignment of the rope

Examining the tug force of both vehicles, the vehicles display newton pair behavior in the x direction, as the surge velocities of both vehicles reach the desired speed of 6m/s. This is denoted in figures 5.13a and 5.13b.

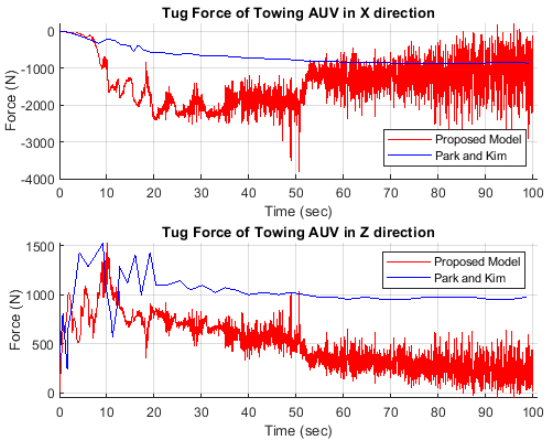

(A) The tug force of the towing vehicle

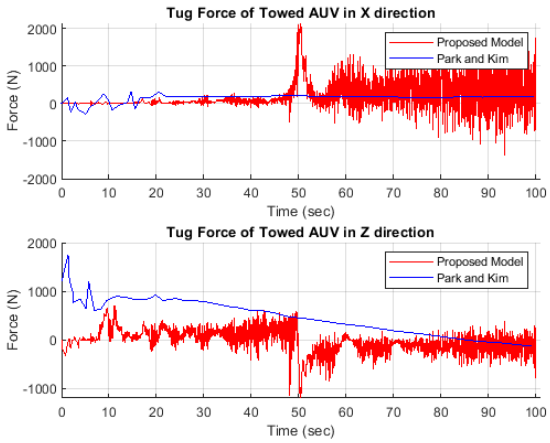

(B) The tug force of the towed vehicle

The results from this maneuver diverge quantitatively from the findings of [23]. Notwithstanding, both models follow very similar trajectories and directions but diverge in magnitude. This divergence can be attributed to the difference in the modeling techniques employed in the rope as well as discrepancies in the material of the rope utilised. Park and Kim employ the finite elements based method, absolute nodal coordinate formulation (ANCF). LMSD, the rope modeling technique used in this work partitions the rope into equal mass points which are connected by spring dampers. The flexibility of the rope is dictated by the rotation angle of each adjacent spring to the mass point. For more

accurate results, this method requires higher number of elements to achieve a rotational angle that reflect the true flexibility of a rope [32]. Contrarily, in ANCF, the absolute positions and gradients of these positions represent the nodal coordinates of elements. The nodal coordinates are defined in a global inertial reference frame so there are no coordinate transformations for the equations of motion. ANCF neglects centrifugal and Coriolis forces in the equations of motion and maintains a constant mass matrix [33][34]. Additionally, LMSD cannot withstand compression as noted in Chapter 4. Corrective measures were implemented to reduce this issue but could still be a contributing factor to the divergence in results.

Examining the cable alignment over time of both models in figure 5.12, the depth of the towed vehicle reduces as the forward speed of the full towing system increases. The extent of increase between both models vary. In our proposed model, the slope of the rope reduces drastically as the towing vehicle begins to accelerate, since the towing vehicle is significantly larger than the towed vehicle and bears all the propulsive capabilities for the system. While the rope in Park and Kim model appears to maintain its steep slope even as the towing vehicle accelerates. The reason for this steeper rope angle may be attributed to the approximation made for the Young's Modulus of the rope used in the proposed work. The Young's Modulus affects the buoyancy of the rope and may have contributed to the difference in rope slope. Additionally, a steeper rope slope features greater drag and should present a slower forward speed and shorter distance travelled but as shown in figures 5.11a and 5.11b, this is not the case for the Park and Kim model.

The proposed model can be modified to bring the cable alignment closer to that of Park and Kim. The approach must focus on first reducing the buoyancy of the rope and then improving the forward speed of the AUV towing system. The density of the rope is increased from the given density of 1300 kg/m^3 to a more typical steel rope density of 7000 kg/m^3. Solely increasing the density results in a more vertical cable alignment shape very close to the Park and Kim model. However, the forward speed of the towing system drastically reduces as expected. The diameter of the rope is reduced by 40% to 0.246m and the thrust of the towing vehicle is increased from 3400N to 5000N. The dynamics of the AUV towing system are preserved with these modifications and present a more vertical alignment of the rope. The cable alignment with these modifications as well as the corresponding vehicle velocities are depicted in figures 5.14, 5.15a and 5.15b

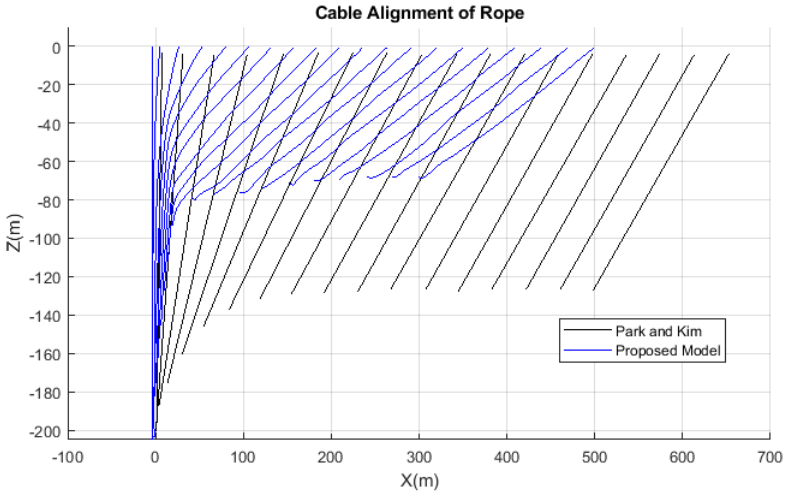

FIGURE 5.14: The cable alignment of the rope when diameter is decreased and rope density is increased

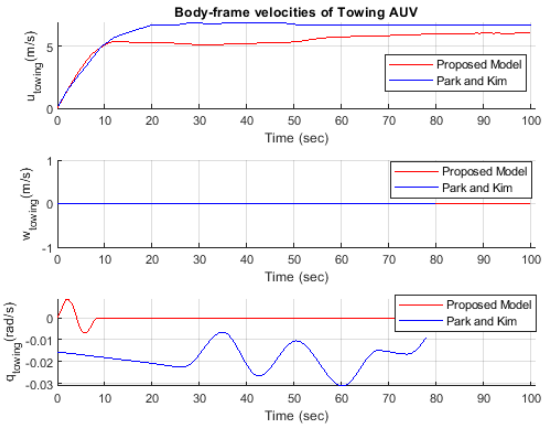

(A) The surge, heave and pitch velocities of the towing vehicle when rope diameter is decreased and rope density is increased

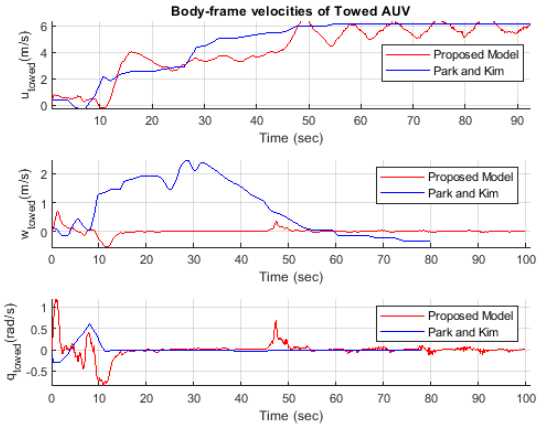

(B) The surge, heave and pitch velocities of the towed vehicle when rope diameter is decreased and rope density is increased

To acquire a comprehensive understanding of the steady state of the system, the system is simulated for an additional 400 seconds to study the behavior of the vehicle a long time after it reaches the desired forward speed. Figures 5.16, 5.17a, 5.17b, 5.18a and 5.18b detail the results of the extended simulation. Once stabilized in the first 100 seconds, the velocities maintain the same pattern for the remainder of the simulation. Similarly do the tug forces. These results reflect that the system is within the steady state region and the dynamic system is stable.

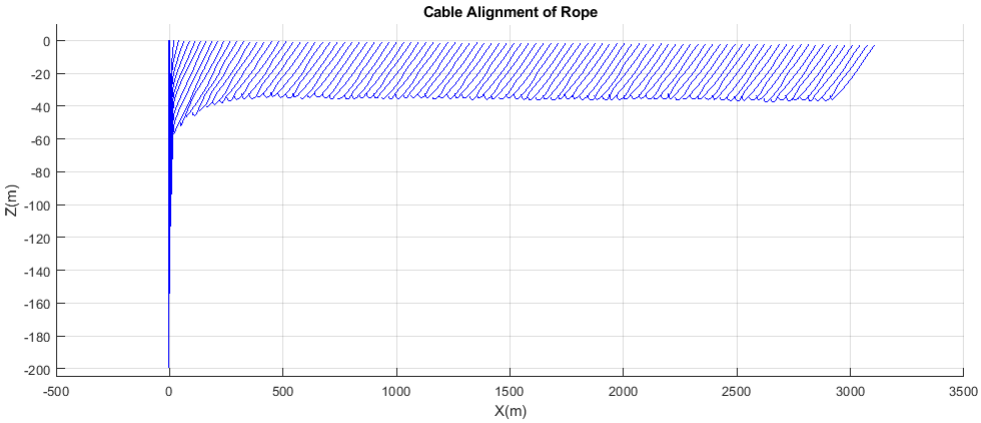

FIGURE 5.16: The cable alignment of the rope for an extended simulation time of 500 seconds

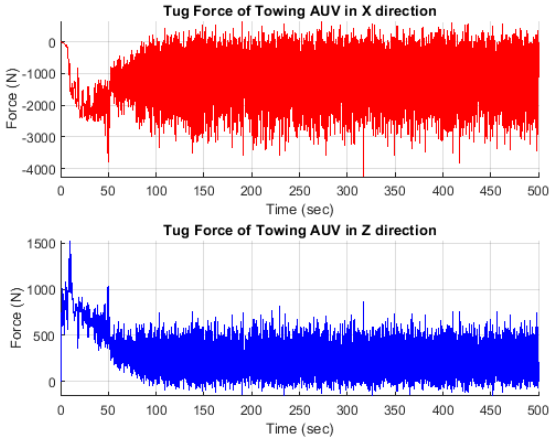

(A) The tug force of the towing vehicle during an extended simulation time of 500 seconds

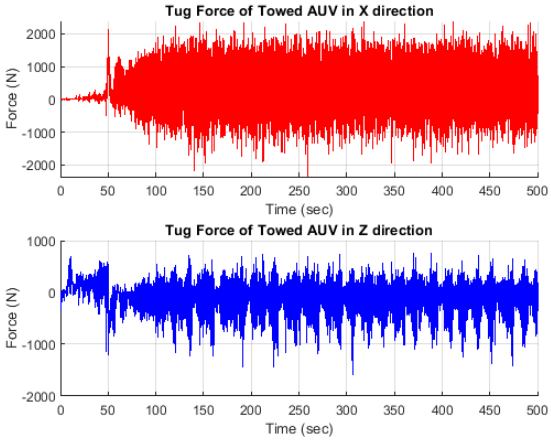

(B) The tug force of the towed vehicle during an extended simulation time of 500 seconds

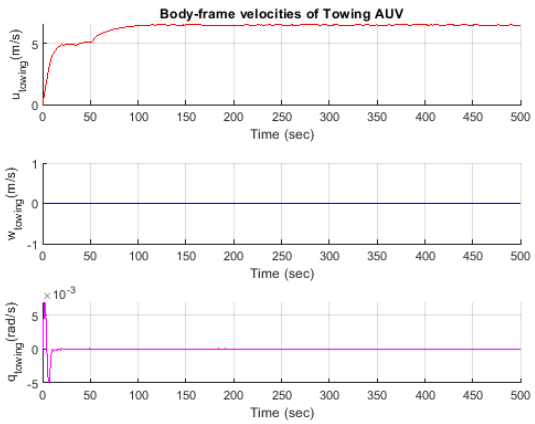

(A) The surge, heave and pitch velocities of the towing vehicle during an extended simulation time of 500 seconds

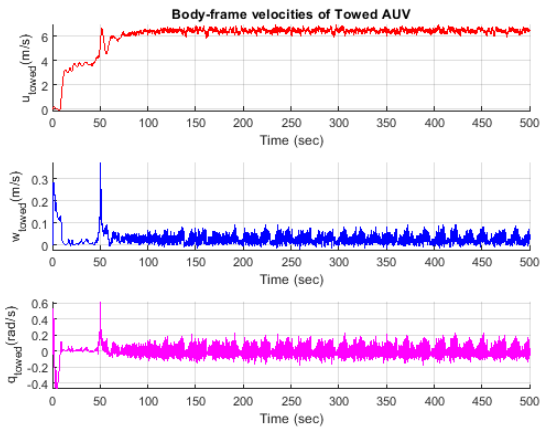

(B) The surge, heave and pitch velocities of the towed vehicle during an extended simulation time of 500 seconds

Chapter 6

Conclusion

This work proposes an AUV towing system in which an AUV tows another AUV of equivalent size using a marine cable. The dynamics of the system are constrained to 3 DOF to study the vehicle in the horizontal and vertical plane. The dynamic equations of this AUV towing system incorporate forces from three components in a loosely couple fashion. The AUVs in this study are assumed to possess top-bottom (XY projection) and port-starboard (XZ projection) symmetry. These symmetry assumptions facilitate the conversion of the hydrodynamic forces and moments from the horizontal plane to the vertical plane. These conversions are executed while observing the sign changes some coefficients must follow due to changes in the direction of the force. The rope is modeled utilizing the lumped mass spring damper method where the mass of the rope is divided into equal mass points across the rope. The limitations of this method include inability to withstand compression and loss of accuracy due to forward euler approximation. Corrective measures are implemented to combat these limitations. These measures include vector path correction for defaulting nodes and adaptive time step adjustment capabilities. Additionally, the catenary curve function for the rope is investigated and compared with the actual trajectory of the rope. The comparison of both curves denotes good agreement and confirms the rope behaves as expected.

The model is assessed for maneuverability according to IMO standards. In the horizontal plane, a straight line test and zigzag maneuver are utilized to evaluate the performance of the model using a scaled version of the Virginia Tech 690 vehicle for both vehicles. In the straight line test, both vehicles are able to achieve the desired surge speed and travel as newton pairs. In the zigzag test, the AUV towing system maintains its course and all the overshoot angles follow the IMO guidelines. In the vertical plane, the maneuver is set up following Park and Kim. Here the vehicles are modeled after the ISimI vehicle with the towed vehicle being considerably larger than the towed vehicle. Furthermore, the towed vehicle is modeled to be a glider and features wings. This maneuver begins with the towed vehicle submerged 200m beneath the towing vehicle. The AUV towing system is able to

accelerate to the desired surge velocity of 6m/s as well as maintain the surge velocity. This work accounts for the heave and pitch motion of the towing vehicle contrary to the model by Park and Kim. This could be a potential source of divergence in the results of our work and that of Park and Kim. Additionally, Park and Kim utilize a different modeling technique for the rope namely ANCF. Creating another possible source for deviation in results.

Research in this area is limited, especially in the aspect of field trials. With this deficit, future work focused on field trials needs to be performed to provide more experimental data. These experimental data for different AUVs could be used to adjust and correct the framework proposed, to accommodate more AUVs with top-bottom and port-starboard symmetry. Furthermore, the model can be extended to study AUVs that do not feature these hull symmetry qualities.

Bibliography

[1] Jun, B.-H., Park, J.-Y., Lee, F.-Y., Lee, P.-M., Lee, C.-M., Kim, K., Lim, Y.-K., and Oh, J.-H., 2009. "Development of the auv 'isimi' and a free running test in an ocean engineering basin". *Ocean Engineering,* ***36***(1), pp. 2–14. Autonomous Underwater Vehicles.

[2] Deutsch, C., 2022. *On the Performance of Long-Range Autonomous Underwater Vehicles: Enhancing the Endurance of AUVs.* TRITA-SCI-FOU. KTH Royal Institute of Technology.

[3] Fernandes, P. G., Stevenson, P., and Andrew, S., 2002. "Auvs as research vessels: the pros and cons.".

[4] Pan, G., Yang, Z., and Du, X., 2013. "Research on dynamic simulation of auv launching a towed navigation buoyage". *Applied Mechanics and Materials,* ***433-435***, 10, pp. 1170–1174.

[5] Miller, L. G., and von Ellenrieder, K. D., 2013. "Modeling and simulation of an auv-towfish system". *2013 OCEANS - San Diego*, pp. 1–9.

[6] Kepler, M. E., Pawar, S., Stilwell, D. J., Brizzolara, S., and Neu, W. L., 2018. "Steering plane dynamics of a small autonomous underwater vehicle that tows a large payload". In 2018 IEEE/OES Autonomous Underwater Vehicle Workshop (AUV), pp. 1–6.

[7] Nelson, R., 1989. *Flight Stability and Automatic Control, Second Edition.* McGraw-Hill.

[8] Stevens, B., Lewis, F., and Johnson, E., 2015. *Aircraft Control and Simulation: Dynamics, Controls Design, and Autonomous Systems, Third Edition.* 10.

[9] Kepler, M. E., 2018. "Dynamics of a small autonomous underwater vehicle that tows a large payload". Master's thesis, Virginia Tech.

[10] Hoerner, S. F., and Borst, H. V., 1992. "Fluid-dynamic lift: Practical information on aerodynamic and hydrodynamic lift".

[11] Li, B., 2016. "Dynamics and control of autonomous underwater vehicles with internal actuators". PhD thesis, Florida Atlantic University, Boca Raton, FL, USA.

[12] Tang, S., 1999. "Modeling and simulation of the autonomous underwater vehicle, autolycus". Master's thesis, Massachusetts Institute of Technology.

[13] Miller, L., Brizzolara, S., and Stilwell, D. J., 2021. "Increase in stability of an x-configured auv through hydrodynamic design iterations with the definition of a new stability index to include effect of gravity". *Journal of Marine Science and Engineering,* ***9***(9).

[14] Chen, C.-W., and Yan, N.-M., 2017. "Prediction of added mass for an autonomous underwater vehicle moving near sea bottom using panel method". In 2017 4th International Conference on Information Science and Control Engineering (ICISCE), pp. 1094–1098.

[15] Arafat, H. N., Stilwell, D. J., and Neu, W. L., 2006. "Development of a dynamic model of a small high-speed autonomous underwater vehicle". In OCEANS 2006, pp. 1–6.

[16] Huang, S., 1994. "Dynamic analysis of three-dimensional marine cables". *Ocean Engineering,* ***21***, pp. 587–605.

[17] Reid, R. O., and Wilson, B. W., 1962. Boundary flow along a circular cylinder. Tech. rep., Texas A and M University, College Station.

[18] Kamman, J., and Nguyen, T., 1990. "A finite segment computer code to simulate the dynamics of towed cable systems". p. 79.

[19] Shan, M., and Shi, L., 2022. "Comparison of tethered post-capture system models for space debris removal". *Aerospace,* ***9***(1).

[20] Raugh, M., and Probst, S., 2019. "The leibniz catenary and approximation of e — an analysis of his unpublished calculations". *Historia Mathematica,* ***49***, pp. 1–19.

[21] Lockwood, E. H., 1961. *Book of Curves.* Cambridge University Press.

[22] International Maritime Organization (IMO), 2002b. "Explanatory notes to the standards for ship maneuverability, msc/circ 1053".

[23] Park, J., and Kim, N., 2015. "Dynamics modeling of a semi-submersible autonomous underwater vehicle with a towfish towed by a cable". *International Journal of Naval Architecture and Ocean Engineering,* ***7***(2), pp. 409–425.

[24] de Barros, E. A., Pascoal, A. M. S., and de Sa, E., 2008. "Investigation of a method for predicting auv derivatives". *Ocean Engineering,* ***35***, pp. 1627–1636.

[25] Triantafyllou, M. S., and Hover, F. S., 2002. "Maneuvering and control of marine vehicles".

[26] Prestero, T., 2001. "Verification of a six-degree of freedom simulation model for the remus autonomous underwater vehicle".

[27] Ferreira, B., Pinto, M., Matos, A., and Cruz, N., 2009. "Hydrodynamic modeling and motion limits of auv mares". In 2009 35th Annual Conference of IEEE Industrial Electronics, pp. 2241–2246.

[28] Njaka, T., 2020. "Design, simulation, and experimental validation of a novel high-speed omnidirectional underwater propulsion mechanism". PhD thesis, Virginia Tech.

[29] International Maritime Organization (IMO), 2002a. "Standards for ship manoeuvrability, resolution msc.137(76)".

[30] Seo, D., 2009. "A study on the underwater glider design based on stability analysis and motion behavior". PhD thesis, Seoul National University.

[31] Thomas, N., and Issac, M. T., 2017. "Analysis of tow cables". *Universal Journal of Mechanical Engineering,* ***5***, pp. 144–149.

[32] Luo, S., Fan, Y., and Cui, N., 2021. "Application of absolute nodal coordinate formulation in calculation of space elevator system". *Applied Sciences,* ***11***(23).

[33] Shabana, A. A., 2015. "Definition of ANCF Finite Elements". *Journal of Computational and Nonlinear Dynamics,* ***10***(5), 09. 054506.

[34] Shan, M., Guo, J., and Gill, E., 2017. "Deployment dynamics of tethered-net for space debris removal". *Acta Astronautica,* ***132***, pp. 293–302.

Appendix A

Appendix A

TABLE A.1: Final Hydrodynamic coefficients for the scaled 690 vehicle

Coefficient	Value	Units
X_{uu}	-8.3869	kg/m
$X_{\dot{u}}$	-4.1	kg
N_{vv}	83.6828	kg
N_{uv}	-133.563	kg
$N_{\dot{v}}$	52.3586	kg
Y_{vv}	-770.7656	kg/m
Y_{uv}	-207.325	kg/m
$Y_{\dot{v}}$	-303.639	kg
N_{rr}	-1575.1188	$kg \cdot m^2$
N_{ur}	-237.2078	$kg \cdot m/rad$
$N_{\dot{r}}$	-343.4242	$kg \cdot m^2/rad$
Y_{rr}	152.083	$kg \cdot m/rad^2$
Y_{ur}	133.563	kg/rad
$Y_{\dot{r}}$	-52.3586	$kg \cdot m/rad$
$Y_{uu\delta}$	30.0818	$\text{kg}/(m \cdot rad)$
$N_{uu\delta}$	-53.4252	kg/rad
$X_{uu\delta\delta}$	-15.6425	$\text{kg}/(m \cdot rad^2)$

TABLE A.2: Final Hydrodynamic coefficients for the ISimI Towing AUV

Coefficient	Value	Units
X_{uu}	-54.7383	kg/m
$X_{\dot{u}}$	-212.6934	kg
M_{ww}	-844.0748	kg
M_{uw}	-2359.8419	kg
$M_{\dot{w}}$	498.2889	kg
Z_{ww}	-4819.9763	kg/m
Z_{uw}	-1459.096	kg/m
$Z_{\dot{w}}$	-5742.3392	kg
M_{qq}	-68175.1722	$kg \cdot m^2$
M_{uq}	-8977.2752	$kg \cdot m/rad$
$M_{\dot{q}}$	-18973.9931	$kg \cdot m^2/rad$
Z_{qq}	-3229.2833	$kg \cdot m/rad^2$
Z_{uq}	-2359.8419	kg/rad
$Z_{\dot{q}}$	498.2889	$kg \cdot m/rad$
$Z_{uu\delta}$	614.1246	$\text{kg}/(m \cdot rad)$
$M_{uu\delta}$	-2336.2435	kg/rad
$X_{uu\delta\delta}$	-319.3448	$\text{kg}/(m \cdot rad^2)$

TABLE A.3: Final Hydrodynamic coefficients for the ISimI Towfish

Coefficient	Value	Units
X_{uu}	-8.8653	kg/m
$X_{\dot{u}}$	-13.8629	kg
M_{ww}	-188.0289	kg
M_{uw}	-390.2094	kg
$M_{\dot{w}}$	6.0269	kg
Z_{ww}	-941.8145	kg/m
Z_{uw}	-895.728	kg/m
$Z_{\dot{w}}$	-382.8108	kg
M_{qq}	-811.1651	$kg \cdot m^2$
M_{uq}	-684.2907	$kg \cdot m/rad$
$M_{\dot{q}}$	-206.2001	$kg \cdot m^2/rad$
Z_{qq}	25.4353	$kg \cdot m/rad^2$
Z_{uq}	390.2094	kg/rad
$Z_{\dot{q}}$	6.0269	$kg \cdot m/rad$
$Z_{uu\delta}$	99.4619	kg/$(m \cdot rad)$
$M_{uu\delta}$	-152.2714	kg/rad
$X_{uu\delta\delta}$	-51.7202	kg/$(m \cdot rad^2)$